LBL-8215

ELECTRON MICROSCOPY STUDY OF MICROSEGREGATION AND DEFECTS IN CZOCHRALSKI GROWN CALCIUM GALLIUM GERMANIUM GARNET SINGLE CRYSTALS

Thomas Franklin Roth
(M. S. thesis)

September 1978

Prepared for the U. S. Department of Energy
under Contract W-7405-ENG-48

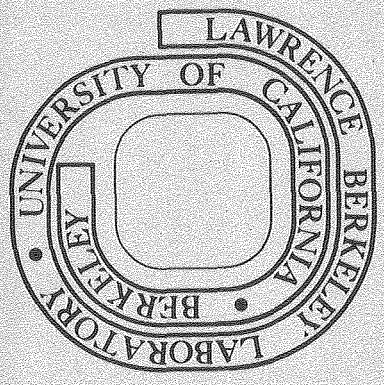

LEGAL NOTICE

ELECTRON MICROSCOPY STUDY OF MICROSEGREGATION AND DEFECTS IN CZOCHRALSKI GROWN CALCIUM GALLIUM GERMANIUM GARNET SINGLE CRYSTALS

Thomas Franklin Roth

Lawrence Berkeley Laboratory
Berkeley, California 94720

ELECTRON MICROSCOPY STUDY OF MICROSEGREGATION AND DEFECTS
IN CZOCHRALSKI GROWN CALCIUM GALLIUM GERMANIUM GARNET SINGLE CRYSTALS

Contents

ELECTRON MICROSCOPY STUDY OF MICROSEGREGATION AND DEFECTS IN CZOCHRALSKI GROWN CALCIUM GALLIUM GERMANIUM GARNET SINGLE CRYSTALS

Thomas Franklin Roth

Materials and Molecular Research Division
Lawrence Berkeley Laboratory
and
Department of Materials Science and Mineral Engineering
University of California
Berkeley, California 94720

Abstract

Microstructural defects in single crystal specimens of calcium gallium germanium garnet (CGGG or $Ca_3Ga_2Ge_3O_{12}$) have been investigated using electron microscopy techniques. High voltage transmission electron imaging and diffraction were used to characterize the observed defects with respect to their morphology, structure, and crystallography. Scanning transmission electron microscopy (STEM) with x-ray microanalysis was employed to determine the elemental composition of certain defects.

Chemical inhomogeneities approximately 0.4μ in size were detected which commonly had dislocations associated with them. These inhomogeneities appear as dark regions in the lighter matrix. They are irregular in shape but most closely approximated by an oblate ellipsoid. They often have a spherical void central to their interior. The inhomogeneities are found to have the garnet crystal structure and contain only elements intrinsic to the CGGG system, being rich in gallium and depleted in germanium relative to the stoichiometric CGGG matrix. The voids are believed to be filled with oxygen gas.

Isolated defects as well as linear arrays were found. The linear arrays of defects were virtually always aligned parallel to <100>

crystallographic directions although arrays along <110> have also been observed.

Several configurations of dislocations in close proximity to the segregate inhomogeneities were common. Despite their physical association with the microsegregates the dislocations are always found to lie in the matrix material and never internal to the micro-segregated regions. Some dislocation lines lying strictly in the matrix were found to have Burgers vectors parallel to <113> directions. Dislocation lines lying at the matrix/microsegregate interface or lying in the matrix but in contact with this interface are also common and are confirmed to have Burgers vectors parallel to <112> crystallographic directions. None of these dislocations showed evidence of dissociation into partial dislocations and are consequently assumed to be perfect.

Dislocation loops lying in the matrix and encircling the microsegregate defects are also observed. These loops are typically about 0.6μ in diameter. The loops are found to be of edge type having Burgers vectors parallel to <100> directions and perpendicular to the {100} planes on which the loops lie. Evidence of dissociation of these loops into partial dislocations whose Burgers vectors are not parallel to <100> directions has been found.

In order to determine the origin of the microsegregate defects and the various dislocation configurations requires understanding the processing history of the Czochralski grown CGGG single crystal boule in conjunction with these microscopy results. The chemical inhomogeneities result from evaporation of germanium from the crystal growth melt and segregation of gallium, which accumulates locally,

in the growing crystal. The evaporation and segregation processes are suggested to be sensitive to thermal fluctuations and gradients in the growth melt as well as processing parameters such as melt composition, growth atmosphere, crystal rotation rate, and crystal pulling rate.

I. Introduction

Much work is currently being done on solid state computer memory elements in which binary information is stored in cylindrical magnetic domains, often called magnetic bubbles.[1,2] Magnetic bubble domains can be supported in thin crystals displaying uniaxial magnetic anisotropy perpendicular to the plane of the crystal. These bubbles can be manipulated via applied magnetic fields and made to translate predictably and reliably within the crystal. This domain mobility, in conjunction with the ability to generate, detect, and annihilate bubbles at specified locations on a fabricated bubble memory chip, provides the computer functions of writing, retrieving, and reading information. Since the magnetic domain is the only moving entity in such an information storage scheme, bubble devices do not suffer mechanical wear problems as do conventional memory systems such as tapes or disks. To obtain economically competitive information storage densities ($\sim 10^6$ bits/cm^2) very thin ($\sim 3\mu$) magnetic crystals are required so that small diameter ($\sim 2\mu$) bubbles are statically and dynamically stable.[3]

Thin films of ferrimagnetic garnets are prime candidates for these bubble memory devices because garnets are found to support bubbles of small enough size and sufficient mobility to provide attractive data storage densities and information retrieval rates.[4] For such applications, single crystal magnetic garnet films are grown on non-magnetic garnet substrates through a liquid-phase epitaxial growth process. The single-crystal substrate not only provides nucleation sites for the growth of the epitaxial film but gives mechanical

strength to the thin and fragile epitaxial layer in a device chip. In addition, the lattice constants of the substrate and epitaxial garnets are controlled such that there is a slight lattice parameter mismatch which results in a stressed induced component to the uniaxial magnetic anisotropy of the epitaxial layer.[5]

Bubble device performance is directly related to the uniformity and perfection of the magnetic film. Static and dynamic properties of bubble domains are altered by magnetic defects in the film. A magnetic defect is a perturbation in the periodic magnetic spin arrangement in the material. The presence of crystal defects implies a discontinuity in the magnetic moment configuration since the forces between atoms in crystals are significantly greater than the forces among spins which maintain their alignment.[6] Thus crystal defects can act as sites for undesirable domain pinning or erratic dynamic behavior. Consequently a defect-free magnetic film is desired.

A prerequisite for the growth of a defect-free film is a defect-free substrate.[3] During the liquid-phase epitaxial growth of the magnetic film on the substrate, any substrate defect which intersects the substrate surface can act as a preferential nucleation site for the magnetic phase. In the case of a substrate dislocation, the disordered core region of the dislocation can permit accommodation of growth units of the magnetic phase in configurations not normally found at undefective (homogeneous) nucleation sites. In this way substrate dislocations can be extended into the epitaxial layer[7,8] with resulting degradation of crystal perfection and device performance. Thus, to insure reliable operation of bubble device chips they must

be fabricated so as to produce relatively defect-free magnetic thin films and this in turn requires a virtually defect-free substrate.

Such garnet substrates have usually been made from gadolinium gallium garnet (GGG or $Gd_3Ga_5O_{12}$). However, recently attention has been drawn to calcium gallium germanium garnet (CGGG or $Ca_3Ga_2Ge_3O_{12}$) because of its superiority over GGG with respect to cost and ease of processing.[9] The relatively low melting temperature of 1380°C for CGGG allows Czochralski boules to be grown from flux melts at a growth temperature about 350°C lower than that for GGG. This permits the use of less expensive platinum (instead of iridium) crucibles. Also, in the CGGG growth process the lower heat input for melting requires one third of the electric power and correspondingly less cooling water than GGG crystal growth. Other commercial advantages arise since GGG is harder than CGGG, and thus the cutting, grinding, and polishing of CGGG substrate wafers from the boules is more easily accomplished. Calcium is also more abundant and cheaper than gadolinium (as is germanium relative to gallium), making CGGG less expensive than GGG. However the smaller lattice parameter of CGGG relative to that for GGG would necessitate development of new ferrimagnetic epi-layer garnet compositions to give the desired lattice parameter mismatch and consequent stress induced magnetic anisotropy needed for device applications.

The CGGG single crystal boules have been grown with relative success using knowledge obtained from the extensive research on GGG crystal growth. At this time, however, defect densities in CGGG are higher than those obtained in GGG crystals. It is hoped that characterization

of microstructural defects in CGGG will suggest ways to optimize processing parameters in order to eliminate the defects. For this reason the objective of this research is to systematically study and characterize microstructural defects in CGGG using electron microscopy techniques.

In the present research two major classes of defects were observed which were distinctly different yet still related. Chemical inhomogeneities in the garnet matrix material were identified and characterized with respect to their distribution, structure, morphology, crystallography, and composition. Associated with these chemical defects were various configurations of dislocations which were characterized with respect to their type, distribution, Burgers vectors, and habit plane (when this was possible).

This work presents the experimental methods and results of these defect characterizations. The results of this study are significant for two reasons. First, microstructure/processing correlations will have a significant impact on the applicability of CGGG in bubble devices. Second, a survey of the literature reveals little published work on systematic defect characterizations in garnet systems at electron microscope resolutions. Consequently the microscopic nature of garnet defects remains virtually unknown. In short, this work is not only of contemporary commercial interest but is also of fundamental academic concern.

II. The Garnet Structure

Investigating defects in garnet materials requires familiarity with the garnet structure. The general chemical formula of garnets is $M_3M'_2M''_3O_{12}$ where M, M', and M'' are metallic cations. In many of the synthetic garnets the metal ions are all trivalent (i.e. +3 charge in $Gd_3Ga_5O_{12}$). CGGG is like the natural garnets in which the cations are of varying size with ionic radii r and occur in different valence states as follows:

Ca	+2	r=0.99Å
Ga	+3	r=0.62Å
Ge	+4	r=0.53Å
(O)	-2	r=1.40Å

Stoichiometry and electroneutrality are maintained by substitution of a +2 and a +4 ion pair for each pair of +3 ions replaced.

The garnet structure belongs to space group O_h^{10}-Ia3d having a unit cell showing body centered cubic symmetry with a typically large lattice parameter (a_o=12.252 in CGGG).[10] The unit cell contains eight $Ca_3Ga_2Ge_3O_{12}$ formula units, giving a total of 8 x 20 = 160 ions per unit cell. Of these 160 ions, 96 are oxygen and it is tempting to describe the structure in terms of the oxygen sublattice. However the oxygens are arranged in neither a simple nor close-packed manner and it is more convenient to visualize their distribution in terms of cation polyhedra.[11] The M cations are surrounded by eight oxygen anions in dodecahedral coordination. The M cation lattice positions are referred to as c sites. A dodecahedron is a distorted cube (Fig. 1A) and c sites provide the least dense packing of oxygen.

Consequently the largest cations usually occupy c sites (calcium in CGGG). The M' sites are the most densely packed with six-fold coordination of oxygen in octahedral symmetry (Fig.1B). These are called a sites and they accommodate small metal cations (Ga) because of the dense oxygen packing. The M'' sites are surrounded by four oxgen atoms in tetrahedral coordination (Fig. 1C) and are called d sites. The d sites have an oxygen packing density intermediate to the a and c sites and are occupied by Ge ions in CGGG.

Each oxygen is shared by four polyhedra (one tetra-, one octa-, and two dodecahedra) as is seen in Fig. 2. The edge lengths of any of the polyhedra are not all equal but the oxygen-cation separation is about equal in each case.[11] The positions of the ions in the unit cell as given by Wykoff[12] are as follows:

Ca: (24c) $\pm$ (1/8 0 1/4; 1/4 1/8 0; 0 1/4 1/8; 5/8 0 1/4; 1/4 5/8 0; 0 1/4 5/8); B.C.

Ga: (16a) (0 0 0; 1/2 1/2 0; 0 1/2 1/2; 1/2 0 1/2; 1/4 1/4 1/4; 3/4 3/4 1/4; 1/4 3/4 3/4; 3/4 1/4 3/4); B.C.

Ge: (24d) $\pm$ (3/8 0 1/4; 1/4 3/8 0; 0 1/4 3/8; 7/8 0 1/4; 1/4 7/8 0; 0 1/4 7/8); B.C.

O: (96H) $\pm$ (x y z; x + 1/2, 1/2 - y, $\bar{z}$; $\bar{x}$, y + 1/2, 1/2 - z; 1/2 - x, $\bar{y}$, z + 1/2; y + 1/4, x + 1/4, z + 1/4; y + 3/4, 1/4 - x, 3/4 - z; 3/4 - y, x + 3/4, 1/4 - z; 1/4 - y, 3/4 - x, z + 3/4); tr; B.C.

The designation B.C. indicates that a body center translation of 1/2, 1/2,1/2 will generate additional lattice points. The oxygen parameters are not rigorously established for CGGG but in other garnets they tend to have values of x=0.04, y=0.05, and z=0.65.

The structure is more easily visualized by considering the unit cell to be made up of eight octants, each octant containing one $M_3M'_2M''_3O_{12}$ formula unit. Considering only one cubic octant, the structure of each octant can be generated as follows: 1) put octahedral (a) sites in a body centered cubic configuration as shown in Fig. 3A; 2) draw non-diagonal bisectors on each of the three mutually perpendicular {100} faces of the octant such that the three bisectors are also mutually perpendicular, i.e. parallel to <100> (Fig. 3B); 3) alternately distribute tetrahedral (d) and dodecahedral (c) sites along these bisectors so as to define a three-fold axis in the octant as shown in Fig. 3C.

This gives the cation configuration of each octant. The eight octants are then distributed in the unit cell so that the arrangement of three-fold axes is as shown in Fig. 4A. This distribution of three-fold axes is obtained by treating each of the face bisectors of the octant (Fig. 4b) as a two-fold axis of rotation. By choosing an arbitrary octant as reference and rotating it by 180° about the two-fold face bisectors, the unit cell can be completely generated as in Fig. 4C.

The bonding in garnets is mostly ionic with some covalent character as is partially reflected in the fact that the cation polyhedra share edges and vertices but not faces. Geller and Gilleo[13] refer to the garnet structure as rather loose since the forces maintaining it are relatively weak and not tolerant of large distortions.

A treatment of crystal defects in the garnet structure must account for the energies associated with the defects. The orderly arrangement of cations in the garnet structure leads to the possibility of many permutations in this order. Variations in the orderly distribution of cations could result from the dissociation of dislocations with faults created. This could lead to a situation in garnets similar to that found in some less complex b.c.c. alloys were dislocation interactions are not solely governed by minimizing the Burgers vector. Instead dissociated dislocations with larger Burgers vectors are observed due to the consequent decrease in fault energies.[14]

Atomic level considerations of fault energies must include not only the electrostatic energy resulting from oxygen displacements but also the changes in anion-cation bond energy associated with the altered cation and anion sublattices. It is reasonable to suggest that the lowest energy defects will be those which leave the least number of ions displaced from their lattice sites. Since the oxygen packing is always disturbed by defects such as dislocations, to a first approximation in garnets the least energy will be associated with defects which leave the most densely packed (octahedral) sublattice unaltered. Defects which leave the b.c.c. sublattice unfaulted result in perturbations of the oxygen packing which can be accomodated by small rotations of oxygen octahedra near the fault plane. For these reasons this discussion of garnet defects is limited to those leaving octahedral sites conserved.

The shortest translation vector of the Bravais lattice is $(a_o/2)\langle 111\rangle$ and is thus suspect as a Burgers vector of dislocations

in garnets. Since the lattice parameter of CGGG is 12.252Å a Burgers vector of $(a_o/2)\langle 111\rangle$ is relatively large with length of $|\vec{b}| = (\sqrt{3}/2)a_o \approx 10.61$Å. Consequently a lowering of energy might be expected from the dissociation of a $(a_o/2)\langle 111\rangle$ perfect dislocation. If the resulting partial dislocations were split with a stacking fault in between, then depending on the energy of the fault, other dislocation dissociations could be energetically favorable also. For example, the elastic energies associated with $(a_o/2)\langle 111\rangle$ and $a_o\langle 001\rangle$ Burgers vectors are not very different ($0.75a_o^2$ and a_o^2 respectively). Depending on the energy of a stacking fault bounded by partials from a dissocated $a_o\langle 001\rangle$ dislocation, the splitting of these dislocations may be energetically favored over dissociation of perfect dislocations with Burgers vectors of $(a_o/2)\langle 111\rangle$.[15]

This discussion assumed that the fault energies associated with such dissociations are not equivalent and it is likely that they are appreciably different. Consider Fig. 5A-C which schematically represent portions of a faulted garnet unit cell with displacement vectors $R_a=(a_o/2)\langle 100\rangle$, $R_b=(a_o/2)\langle 110\rangle$, and $R_c=(a_o/4)\langle 111\rangle$ respectively. Inspection of these figures shows that the orderly distribution of the tetrahedral and dodecahedral sites is disrupted by each of these displacements, which could result from the dissociation of perfect dislocations. It can also be seen that each kind of defect leaves the octahedral sublattice unaltered in accordance with the basic assumption. However, an important difference can also be seen.

The displacements $(a_o/2)\langle 100\rangle$ and $(a_o/2)\langle 110\rangle$ of Figs. 5A and 5B are equivalent to exchanging positions of tetrahedral and

dodecahedral cations. The octahedral (Ga^{3+}) and tetrahedral (Ge^{4+}) ions in CGGG are of similar size but vary in valence. Dislocations having Burgers vectors of $(a_o/2)\langle 100\rangle$ and $(a_o/2)\langle 110\rangle$ would therefore be expected to have electrostatic as well as elastic contributions to their total energy.

On the other hand, Fig. 5C illustrates that a displacement of $(a_o/4)\langle 111\rangle$ does not merely result in an exchange of lattice sites. Such a displacement will cause initially empty sites in the regular garnet lattice to be filled and cations bounding the fault plane will be brought into much closer proximity. Such displacements can be visualized as a non-stoichiometric addition or removal of a crystal slice, and the energy associated with such a defect will have an appreciably different electrostatic contribution than that of a defect causing only disordering of the cation sites.

The differences between electrostatic and strain energies associated with the various defect displacements promote a variety of possible perfect and dissociated garnet dislocations. Experimental observations of splitting widths of garnet stacking faults with definitive Burgers vector determinations could give considerable insight into the types of atomic level interactions which influence the existence of particular defect configurations.

III. Specimen Preparation

A. Czochralski Grown CGGG Single Crystals

The CGGG single crystals used in this study were provided by Philips Laboratories of Eindhoven, Netherlands. Crystal growth procedures were as follows.[16] Powders of 99.99% purity $CaCO_3$, Ga_2O_3, and GeO_2 were obtained from Merck (Darmstadt, Germany), Alusuisse (Neuhausen, Switzerland), and Hoboken (Hoboken, Belgium) respectively. The starting powder mixture had composition Ca:Ga:Ge=73.2:24.8:38 atomic percent. Three hundred (300) grams of the mixture was homogenized with 120 ml of ethanol in an agate ball mill for 30 minutes. Cylindrical tablets 50 mm in diameter were pressed from the dried mixture and fired 16 hours at 900°C to expel carbon dioxide and volatile impurities.

Fired tablets for the Czochralski growth melt were placed in a platinum crucible 50 mm high, 50 mm internal diameter, and with 1 mm thick walls. The r.f. heated crucible was insultated with 3 mm zirconia felt and 5 mm alumina. Covering the crucible was a lid with a 25 mm diameter hole at its center. The powder mixture was heated and equilibrated near 1380°C (the melting point of CGGG).

Isothermal growth of Czochralski single crystals was accomplished using a rotation rate of 55 RPM and a pulling rate of 5 mm per hour. Cooling to room temperature after completion of crystal growth was done in two hours.

Two complications were incurred during the growth of the CGGG single crystals.[9] An appreciable amount of evaporation occurred, forming a white deposit on the pulling shaft. The deposit was determined

to be pure GeO_2 by x-ray diffraction. As a result of the evaporative loss of Ge the composition of the growth melt changes from its original ratio via Ca:Ga:Ge=37.5:25:37.5 to the final compositional atomic percent ratios Ca:Ga:Ge=37.8: 25.2:37. The rate of loss of Ge from the melt was subsequently found to be sensitive to temperature and oxygen partial pressure, with decreased evaporation at lower temperatures and higher oxygen partial pressures.

The second complication that occurred during crystal growth was solid state precipitation in the crystal. Although $Ca_3Ga_2Ge_3O_{12}$ is normally clear the single crystals often contained white opaque regions. These regions were shown by x-ray topography to consist of decorated linear defects. The decoration consisted of 100 μm long linear arrays of small globules. In addition clear seed crystals appeared to become opaque during the growth process. The defects were not characterized further.

In an effort to minimize these complications several adjustments were made to the growth procedure.[9] Varying the crystal rotation rate between 27 and 55 RPM did not eliminate the linear defects. The evaporation of Ge could be limited but not eliminated by restricting the ventilation of the space over the melt surface and by admitting a high oxygen partial pressure. However, placing an alumina housing over the hole in the crucible lid to create an isothermal environment for the growing crystal and to permit pressure build-up of the volatile gases did not improve crystal quality significantly. Likewise varying oxygen partial pressure from 0 to 760 torr in the normal 760 torr imposed nitrogen atmosphere above the melt did not improve crystal

quality significantly. The investigators[9] note that local overheating of the melt should be avoided to grow high quality crystals since GeO_2 evaporation is so sensitive to temperature.

B. Transmission Electron Microscopy Specimen Preparation

A boule of $Ca_3Ga_2Ge_3O_{12}$ approximately 4 cm long and 2 cm in diameter was supplied by Philips Laboratories, Eindhoven, The Netherlands. TEM specimens were prepared as follows:

1) Slices approximately 10 mils thick were cut perpendicular to the boule axis. The boule axis was parallel to <001>.

2) Discs 3 mm in diameter were cut ultrasonically.

3) The discs were mounted on a glass slide with a low melting point (~150°C) resin and mechanically thinned on 600 grit emery paper until the specimen was 1.0 mil thick (as measured using a micrometer).

4) The thinned specimen was dissolved off of the slide using ethyl alcohol and carefully transferred to a 3 mm diameter copper grid which was lightly coated with epoxy glue.

5) After allowing the epoxy to dry, the specimen was ion milled until electron transparent regions were detected. Typical ion thinning parameters were:

a. 5 kV accelerating potential for argon ion guns

b. 25 μA ion beam current

c. 25° angle of impingement

d. as long as 80 hours of thinning time were required, with a typical duration of 55 hours.

Attempts to expedite ion thinning of specimens resulted in samples unsuitable for TEM studies. Specimens were thinned for about 16 hours with an accelerating voltage of 9 kV, ion beam current of 40 μA and an angle of impingement of 25°. After this the voltage was reduced to 6 kV, the beam current to 30 μA, and the thinning angle to 15° in an attempt to produce a central hole in the specimen having thin edges and free of ion induced damage. After about 5 more hours of thinning under these conditions the specimens were found to have no central hole but many small perforations with edges too thick to permit adequate electron transmission.

Before observation in the electron microscope, a layer of carbon approximately 40Å thick was vacuum evaporated onto one surface of each specimen to remedy problems associated with electrostatic charge build-up in the insulating crystals while in the electron microscope.

IV. Electron Diffraction and Imaging

This section deals with the practical problems encountered and procedures used in the course of the transmission electron microscopy experimentation. High voltage transmission electron microscopy (HVEM) was performed using the Lawrence Berkeley Laboratory Hitachi HU 650kV instrument equipped with a high angle ($\pm 20^{o}$) double tilt goniometer stage. HVEM permits the use of thicker ion-milled CGGG specimens because of the increased penetration at high voltages and facilitates high order bright field imaging for increased resolution of lattice defects.[17] High order bright field imaging is especially applicable at high voltages due to the flatness of the Ewald sphere permitting excitation of high order reflections through careful specimen tilting. The image is formed using the transmitted beam while a high order diffracted beam $n\vec{g}$ is excited (usually n=4 in this study). Since background intensities are high under such conditions focussing is easy and exposure times are short, minimizing loss of image resolution due to mechanical or other instrument instabilities. Image detail and resolution, such as those of dislocations[18], are improved because of the long extinction distance (ξ_g) associated with high order reflections and the dependence of image width on $(1/s\xi_g)$.[19] The deviation parameter s can be altered by tilting the specimen and monitored by observing the Kikuchi line near the operating high order reflection. Increased resolution of lattice defects such as dislocations can occur (depending on $\vec{g}$, specimen orientation, and electron wavelength λ) if s is slightly positive, i.e. the Kikuchi line lies outside of the

operating reflection as is seen in the inset diffraction pattern from the high order bright field micrograph of Fig. 6A.

Weak-beam dark field imaging is another specialized technique permitting increased resolution of lattice defects and easier image interpretation.[20] Weak-beam images are obtained by forming a dark field image using a first order Bragg reflection $\vec{g}$ when the crystal is oriented such that the high order refection $n\vec{g}$ ($n > 1$) is operating. This effectively increases the deviation parameter s of the imaged reflection and results in increased resolution since diffraction contrast arises only at the core of defects such as dislocations.[21] Ease of specimen tilting to excite high order reflections is again facilitated at high voltages making weak-beam imaging a valuable technique of HVEM.

The advantages offered by weak-beam and high-order bright field imaging are qualitatively illustrated in Fig. 6. A specimen of $Ca_3Ga_2Ge_3O_{12}$ is imaged at 650kV in the sequence of micrographs and evidence of dislocation lines around chemical microsegregates can be seen. The improved resolution of dislocation images is apparent in the high-order bright field and weak-beam dark field images of Figs. 6A and C respectively as compared to the conventional bright field image of Fig. 6B. These techniques giving increased resolution of lattice defects were utilized often in this study of defects in CGGG and circumvented some of the dynamical contrast phenomena which hindered interpretation of images for other investigators in studies of different garnet systems.[22,23]

Diffraction patterns obtained from undefective CGGG matrix regions often displayed "extra" spots as can be seen in Fig. 7. A symmetrical

[100] cubic diffraction pattern is indexed in A, and it is clear that <200> type reflections are present. This is confirmed by calibration of the microscope camera constant ($\lambda L=rd$) using a ring pattern obtained from a polycrystalline gold standard foil and shows correspondence with <200> type interplanar spacing. Upon tilting the specimen away from the [001] pole to obtain either of the mutually perpendicular high-order two beam cases shown in B or C of Fig. 7, some spots having <200> periodicity are seen to disappear. Structure factor rules for the garnet crystal structure[24] show n<200> where n=odd integers to be unallowed reflections. The appearance of these unallowed systematic reflections in symmetric diffraction patterns from a variety of major poles could be accounted for by double diffraction. Dark field imaging of the unallowed spots gave no evidence that they arose from second phases, microstructural defects, or anything other than double diffraction. Extra double diffraction spots are not normally observed in patterns from perfect crystals. However in the diamond cubic and hexagonal close-packed structures extra spots can be observed.[25] This is the case also for the complex b.c.c. type structure of CGGG. In the example of Fig. 7A, the <200> type spots occur by double diffraction among <420>, <422>, and <400> reflections. These reflections are the three strongest reflections as listed on the ASTM card[10] for $Ca_3Ga_2(GeO_4)_3$ having I/I_1 values of 100, 65, and 65 respectively. Thus extra spots in the symmetric diffraction pattern occur at positions which are the vectoral sums of strong allowed diffraction vectors, i.e., if $\vec{g}_1 = <420>$ and $\vec{g}_2 = <\bar{4}00>$ then double diffraction and the resultant sum $\vec{g}_1+\vec{g}_2=\vec{g}_3=<020>$ gives rise to a spot in the normally unallowed

<020> position. Upon tilting to the systematic row or two beam cases such as Fig. 7B and C the <200> type reflections disappear since at least one of the contributing allowed reflections is no longer strongly diffracting. While double diffraction is a viable explanation for the observed phenomena it should be noted that extra <200> type spots in [001] type patterns from silicon[26] have been attributed to dynamical effects among successive Laue layers in the diffraction pattern reciprocal space. It is important to distinguish between such anamolous appearances of reflections and other causes such as diffraction from second phase particles.

V-A. Microsegregate Defects/Results

Chemical inhomogeneities in the CGGG samples could be identified by their dark contrast against the lighter matrix in TEM micrographs. Two closely-spaced defects of this type are imaged in bright field at 650kV in Fig. 8. The interface between the defective region and the matrix is sharp and shows no evidence of dislocations despite being obscured by the encircling periodic lobes of intensity. In the sequence of Fig. 8A-D the operating diffraction $\vec{g}$ vector rotates clockwise in the plane and the lobes of contrast distort so as to tend to maintain a line of no contrast perpendicular to $\vec{g}$. The lobes are also seen to overlap in the region between the two chemical defects where the periodic intensity variations are interrupted. The projected shape of each inhomogeneity, as is best seen in Fig. 8B, is approximately elliptical with major and minor axes of lengths 0.25μ and 0.20μ respectively. The defects are situated such that their major axes are nearly colinear. Bright field stereomicrographs indicate these defects to consist of an oblate ellipsoidal volume which can be generated by rotating the projected elliptical area about the major axis of the ellipse.

Lobed "butterfly" contrast of this sort is generally attributed to a coherent lattice imperfection which strains the matrix.[27] Strain contrast can be described in terms of a displacement vector $\vec{R}$ due to the local altering of the matrix by the imperfection. No contrast arises where $\vec{g}\cdot\vec{R}=0$, giving a line of no contrast perpendicular to $\vec{g}$ for a spherically symmetrical strain field. Qualitative treatment of the strain contrast from the defects of Fig. 8 confirm these to

not be strictly spherical but rather ellipsoidal. The periodic intensity variation is absent in the region between the defects where the strain fields overlap and the displacement vector $\vec{R}_1$ due to one defect is about equal in magnitude but opposite in direction to the displacement vector $\vec{R}_2$ of the other closely-situated defect.

The region marked K in Fig. 8A is representative of microstructural features commmonly encountered in the CGGG samples. Such defects were often in close physical proximity to the chemical inhomogeneities although they could also be found in otherwise undefective CGGG matrix material. Contrast behavior from such features was quite sensitive to diffracting conditions and specimen orientation. Sometimes fringed contrast was observed in such defects although the fringe intensity variation and orientation relative to $\vec{g}$ showed no consistent behavior. It was not possible to make these defects go out of contrast by tilting the specimen. This contrast behavior led to the belief that these were not dislocations or internal boundaries like twins or stacking faults. Combined with the observation that cracks radiating from the ion milled hole in the specimen showed similar contrast, it is safe to assume that such features are cracks in the material. The origin of such cracks is not known and was not studied, so they will not be mentioned further except to be identified as cracks also designated K in subsequent micrographs.

Another morphology of the chemical inhomogeneities was also commonly observed. The bright field micrograph of Fig. 9 shows such defects to appear as dark regions about 0.4μ in size in a lighter matrix, but a light circular patch about 0.15μ in diameter is seen central

to the interior of the inhomogeneity. The interface between the matrix and defective region is again quite well defined. However no evidence of strain contrast is apparent in the vicinity of the defect.

Bright field stereomicroscopy of such defective regions shows the dark area to have a shape similar to a cylinder but with an irregular non-circular cross section. Steromicrographs establish the light patch to be nearly spherical in shape and situated close to the geometrical center of the dark region. The matrix/defect interface is found to be curved and not crystallographic or facetted in nature.

Figure 10 shows another such chemical inhomogeniety with the light circular patch in a thin area of an [001] oriented specimen as imaged in bright field. Evidence of dislocations can be seen in the regions designated d. Rigorous analysis of such dislocations is reserved for a subsequent section. The dislocations are located at each corner of the defect and are in contact with the matrix/defect interface. This interface appears facetted with the projected interface image lying almost parallel to <110> type directions. The circular patch is slightly displaced from the center of the defective region and is seen to consist of two concentric annuli of different intensity denoted s and m. Inside the region bounded by ring s the transmitted electron beam passes undisturbed, i.e. as through a hole. This concentric ring contrast is consistent with the notion that this feature is spherical in shape provided it is also hollow. Thus the inner annulus s is the projection of where the sphere is cut by the surface of the specimen and the outer annulus m is where the sphere reaches its widest equatorial dimension within the middle of the specimen. The region within ring

s is most intense since the transmitted beam passes without encountering any material, while a slightly darker intensity gradient is detected between rings s and m due to the varying thickness of material encountered by the electron beam in that region.

The two morphologies of chemical inhomogeneities just described were observed often in the course of this study and the following differences were generally maintained: (1) inhomogeneities with spheres near their centers showed evidence of dislocations in close proximity yet never internal to the chemical defects, (2) inhomogeneities with spheres and dislocations do not show pronounced strain contrast, and (3) inhomogeneities without spheres (and without dislocations) do display the lobed strain constrast which changes predictably with variation of diffracting conditions.

Despite these stated differences, certain similarities were consistently maintained by the two types of inhomogeneities. A general observation was that the dark, chemically inhomogeneous region was always darker than the matrix in both BF and DF and independent of the diffracting conditions. This is verified by the BF/DF pair of Fig. 11 which shows that inhomogeneities (with or without the central sphere) appear dark against a lighter matrix. The spherical entity is also seen to appear as a circular patch lighter in contrast than the matrix in both BF and DF.

Another feature common to the two types of inhomogeneities is that electron diffraction patterns taken from either type of defective region are identical to patterns taken from the undefective CGGG matrix. No extra spots or streaks are resolved in the patterns, nor are any

spots deleted. While extra spots were observed in symmetric diffraction patterns obtained near major crystallographic poles, they could be accounted for by considering double diffraction phenomena as explained earlier. In addition, these extra spots in symmetric selected area diffraction patterns arose irregardless of whether the area selected was undefective matrix material or whether a chemical inhomogeneity was within the SAD aperture. Furthermore, rigorous dark field imaging of diffracted beams in several samples and various orientations failed to reveal any diffraction spots attributable solely to a chemical inhomogeneity. Based on this electron diffraction evidence the defective regions are believed to maintain the garnet crystal structure.

The density and distribution of these inhomogeneities are difficult to generalize. Electron microscope observations revealed that the distribution of defects varied from region to region even within a single TEM sample. The defects tend to be localized, i.e., it was common to observe highly defective areas approximately 10μ in diameter containing on the order of 100 such defects adjacent to areas 10μ in diameter which were completely undefective. Examples of defect densities spanning the entire range just established could also be found depending on the particular specimen selected and the area viewed. Despite the finding that undefective garnet matrix regions having dimensions as large as 50μ could be traversed in the electron microscope, the chemical defects observed in the CGGG samples can be qualitatively described as prolific.

In regions of relatively high defect density the chemically inhomogeneous regions could be found to be distributed in a variety

of ways. Often the inhomogeneities appeared to be randomly distributed in the matrix, but ordered distributions were also common. Figures 12A and B show adjacent regions in a [001] oriented CGGG specimen as imaged in BF. Examples of inhomogeneities with and without a central sphere can be found and the distribution of defects in the matrix is obviously not random. Linear arrays are observed aligned parallel to the mutually perpendicular <100> crystallographic directions in the plane of the page. Although arrays aligned parallel to <110> were also observed in some areas, alignment parallel to <100> was much more common. In the micrograph of Fig. 12A a chemical defect with a central sphere is seen at S. This defect is bounded by semi-circular arcs having a line of no contrast perpendicular to the operating $\vec{g}$. This is suggestive of the contrast obtained from prismatic edge dislocation loops having Burgers vectors normal to the plane of the loop and a line of no contrast where $\vec{g}.\vec{b}\times\vec{u}=0$ ($\vec{u}$ being a vector parallel to the dislocation line direction). Such dislocation loops are discussed in detail in a later section but it should be noted that the observation of such a loop is consistent with the generalization that defects having a central sphere often have dislocations in close proximity to them but no strain contrast is displayed.

Lobed strain contrast associated with the inhomogeneities not having a central sphere can also be seen in Fig. 12. It is most apparent in the region L of Fig. 12B where evidence of strain field overlap is visible around the linear array of closely spaced defects. In the region L as well as elsewhere a very faint yet detectable line of light contrast is seen connecting the defects, running parallel

to the <100> axis of defect alignment and through the centers of the defects. Detailed tilting of the specimen was not performed to determine if the extra intensity is due to diffraction contrast from the overlapping strain fields.

The observation of linear arrays of defects in TEM samples aided in identifying defects by optical microscopy in 10 mil thick slices cut from the sample boule perpendicular to its growth axis. Using transmitted light and magnifications of 600x, white opaque regions were locally distributed randomly as well as in linear arrays. Since individual regions were of an appropriate size (i.e. 0.5 mm at 600x) they are believed to be the same chemical inhomogeneities observed in the electron microscope. The distribution of these defects as established by optical microscopy confirms the TEM findings that defects tend to be prolific but localized; they occur in random or linear arrangements, and localized regions of undefective matrix are also common. Furthermore, it was qualitatively established that defect densities and configurations did not vary significantly in regions close to the boule growth/rotation axis as compared with regions near the periphery of the boule. Defect densities as a function of length along the boule axis were not established by optical nor TEM methods.

V-B. Microsegregate Defects/Discussion

The two types of chemical inhomogeneities which have been observed (with and without the central sphere) are believed to be the same type of defect except at different stages of development. This is supported by the similarities in size, shape, and contrast displayed

by each as well as the observation of both types of defects interdispersed in linear arrays.

Both types of defects appear as dark regions in the lighter matrix in both BF and DF, suggesting that the defective regions exhibit greater absorption of electrons in both transmitted and diffracted beams than does the CGGG matrix material. Since the electron diffraction evidence suggests that the defects have the same garnet structure as the matrix, this contrast could arise from a compositional difference between the matrix and the defect. Such a compositional variation tends to alter the intensity of beams passing through the material in two ways as follows: (1) by introducing different atomic scattering factors $f(\theta)$ into the structure factor (F_g) summation, and (2) by variations in unit cell volume V_c. Thus compositional changes can cause intensity variations since the amplitude ϕ_g of an electron wave is proportional to F_g/V_c and the intensity is proportional $\phi_g \phi_g^*$.[27] Since absorption seems significant in interpreting the contrast from the defects and since electron absorption cross sections generally increase with increasing atomic number, it is tempting to think that the dark contrast arises from replacing some of the elements in the CGGG matrix with elements of higher atomic number in the defective regions. On this premise it is suspected that the dark region is rich in Ga or Ge since for typical reflections used ($\sin\theta/\lambda$=0.6-0.7) the atomic scattering factors for these elements are about 1.5 times as large as that for Ca.[27] However this qualitative notion is subject to shortcomings because it fails to quantitatively account for the actual lattice positions which such substitutional atoms occupy in the unit cell and how electron wave

amplitudes and intensities will be affected by constructive and destructive interference phenomena when the atomic scattering factors and atomic positions are incorporated into the structure factor calculation. Therefore the observed contrast could result from differences in garnet-structure lattice site occupation between the defect and matrix although the compositional nature of this difference cannot be deduced from contrast behavior alone. Compositional variations between matrix and defective garnet regions can also account for the observed strain contrast due to lattice mismatch since garnet lattice parameters are sensitive to substitution of elements.

The light contrast displayed in both BF and DF by the spherical feature central to some of the chemical inhomogeneities can be explained in a reverse manner, that is the sphere is composed of material which allows greater electron transmittance. The spherical morphology is indicative of a hydrostatic pressure such as that exerted by entrapped gas. All of the above observations can be explained if the sphere is assumed to be filled with oxygen gas under pressure. The spherical morphology and hollowness follow as a direct consequence while the light contrast is explained in terms of the low atomic number and hence small absorption cross section of oxygen permitting greater transmittance of the electron beams. The source of this accumulated oxygen could be the constituent oxides in the crystal growth melt itself or the atmosphere of 760 torr oxygen pressure imposed above the melt during growth.

A specimen was observed at 650 kV in a Hitachi HU650 electron microscope equipped with a heating stage. No dimensional changes

were detected in the chemical inhomogeneities or internal spheres which were imaged before and after heating for 4 hours at 650°C. Heating to higher temperatures is expected to cause enlargement of the oxygen filled sphere since oxygen pressure could then overcome the surface energy tending to reduce the surface area (and hence the volume) of the sphere. Temperatures near the CGGG melting point of 1380°C are suggested.

The nature of the matrix/defect interface has been deduced from the observation of strain and dislocations. The interface is always very distinct and it is considered to be coherent for inhomogeneities showing strain contrast while coherency is partially lost when dislocations are generated in the matrix near the interface and the evidence of strain is greatly reduced. The sharpness of the interface implies a very strong short range force maintaining it and a chemical force is suspected. Attempts to further characterize the interface using direct lattice imaging have not succeeded due to complications from excessive contamination of the specimen in the electron microscope as well as insufficiently thin ion-milled specimens.

Observation of strain fields around some of the defects can be correlated with the linear alignment of the chemical defects. Similar practical observations of aligned precipitate particles have been made in other systems[28] with the comment that the transformation of one particle tends to cause the transformation of neighboring particles along certain crystallograhic directions. An elastic interaction between the chemical inhomogeneities is likely since they are separated by distances comparable to their diameter and evidence of overlapping

strain fields has in fact been observed (Figs. 8 and 12). Nabarro[29] cites unpublished work by Crum which showed that there was no interaction between centers of dilatation in isotropic crystals and that the dilatational stress field of one coherent particle does not affect the energy needed to form another similar particle nearby. This indicates that since interaction between strain centers is observed, the cubic garnet structure of CGGG is not isotropic.

Cahn[30] has considered the interaction of dilatational strains in elastically anisotropic cubic crystals and the pertinence of strain energies to nucleation in solids. He gave a mathematical treatment showing that the strain energy associated with a particular point in a small transformed volume depends on the strain at that point as well as strains at other points in the volume and the strains due to all other particles in the system. Using this approach Cahn concluded that, given a pre-existing precipitate particle, it is energetically favorable to nucleate a second particle in an elastically soft direction. Furthermore, the relative values of the material elastic constants determine the soft direction and if $2C_{44}-C_{11}+C_{12} > 0$ then alignment of particles will occur along <100> (while if $2C_{44}-C_{11}+C_{12} < 0$ then alignment parallel to <111> is favored). The observation of linear arrays parallel to <100> directions in CGGG indicates the former condition to be true of the elastic constants for CGGG. Cahn[30] suggests that <100> directions are also favored in most metallic systems, and the elastic constants of several garnets indicate that <100> alignment would be favored although the elastic constants for $Ca_3Ga_2Ge_3O_{12}$ are not available.[31]

Cahn's treatment was extended to consider a particle with two neighbors of equal size and at equal distances, but with one neighbor in a hard direction and the other in a soft direction. Due to free energy considerations the particle in the soft direction will have a lower solubility in the matrix than the particle in the hard direction and hence is more stable. As a result, even if particles initially nucleated and grew at random then this enhanced stability would dictate the development of an ordered array, i.e. a simple cubic pattern if <100> directions are soft. Thus it is possible that the observed alignment of the chemical inhomogeneities is a post-nucleation phenomena whose driving force is derived from strain energy. This is not in agreement with the studies of microsegregation in CGGG reported by Mishra and Thomas[32] who suggest such linear defect arrays to form on existing dislocation lines which act as pipes for easy segregate diffusion.

Linear arrays of interspersed defects with and without the central sphere were common as was mentioned previously and can be seen in Fig. 12A and B. Since alignment of defects is attributed to the strain field interactions between neighboring inhomogeneities and inhomogeneities showing pronounced strain effects generally did not have a central sphere, it is reasonable to conclude that alignment of defects occurs due to strain interactions among defects not having a central sphere. However, defects having a central sphere and not exhibiting significant strain are also observed in the linear arrays indicating that formation of a sphere is a post-alignment process. This is not to say that a defect must occur in a linear array in order

to form a sphere because many instances of defects with spheres (as well as their associated dislocations) isolated in otherwise undefective matrix have been encountered. Instead it is suggested only that the strained chemically inhomogeneous regions not having a sphere are a preliminary stage in the formation of the defects which have developed the central oxygen-filled sphere. A qualitative model for sequential defect transformation stages and their relation to crystal growth melt conditions and processing parameters is included in the last section of this paper.

VI-A. Chemical Analysis/Results

Chemical micro-analysis of the inhomogeneous regions was performed using scanning transmission electron microscopy (STEM) with energy dispersive analysis of x-rays (EDAX). Limited access to chemical micro-analysis equipment was gained by traveling to Rockwell Science Center in Thousand Oaks, California to use their Philips 400 transmission electron microscope equipped with a Philips scanning electron imaging unit. A lithium-drifted silicon detector manufactured by Nuclear Semi-Conductor was used for counting x-rays, and the resulting numerical data was processed using a Tracor/Northern NS 880 analyzer. The identical CGGG samples used in HVEM studies were used for this analysis. Chemical inhomogeneities both with and without the central sphere were investigated using a 200Å diameter probe of 120keV electrons. The experimental procedure and results are shown schematically in Fig. 13. The electron probe was first placed in an otherwise undefective CGGG matrix region about one micron away from a chemical defect and spectral counts were recorded for a counting period of 200 seconds. Chemical information was recorded as digitized spectra (counts of a particular energy versus energy) on computer printout as well as polaroid pictures of a CRT graphic display (see Fig. 14). This process was repeated with the 200Å probe central to the dark chemical defect. In the case of chemical defects having a central sphere the probe was placed on the middle of the dark annular region which encircles the sphere (see Fig. 13). Altogether four different chemical defects were investigated, two with and two without the central sphere, and their corresponding matrix spectra were also each

recorded. Spectra were also recorded with the probe placed central to the light area of the sphere for both of the defects displaying a sphere.

Qualitative analysis of the K_α peaks of the resulting spectra showed several consistent results as follows: (1) All matrix and defect regions showed evidence of only five elements, those being Ca, Ga, Ge, and smaller amounts of Fe and Cu. No oxygen was detected since the STEM/EDAX unit will not resolve species having atomic number less than eleven. (2) All defect spectra showed the relative heights of the K_α peaks for Ga and Ge to be reversed with respect to their corresponding matrix spectra, i.e., the Ge peak was more intense than the Ga peak in matrix spectra whereas the Ga peak was more intense than the Ge peak in spectra from the chemical defects. (3) Spectra obtained with the probe placed central to the spheres showed inconsistent and uninterpretable behavior.

Quantitative analysis using the method of Goldstein, et al.[33] was done by manually replotting the digitized spectra so that the areas under the K_α peaks could be more accurately calculated for each of the matrix and defect regions. The data generated is tabulated in the appendix where the analytical procedure is also outlined. Three assumptions were made in the analysis: (1) the area under a peak for a given element is directly proportional to the number of atoms of that element present in the volume of material from which chemical information is being received, (2) the matrix material is stoichiometric $Ca_3Ga_2Ge_3O_{12}$, and (3) the defective region is a garnet of composition $Ca_xGa_yGe_zO_{12}$ where cation sites are conserved with

64 cations per unit cell or 8 cations per formula unit. Therefore, by taking the appropriate ratios of areas under the peaks from matrix regions and comparing with the stoichiometric cation atomic fraction ratios it was then possible to deduce a nominal composition of the defective regions from the ratios of the area under their STEM/EDAX spectra peaks.

The calculated composition $Ca_xGa_yGe_zO_{12}$ of the chemically defective regions is given in Table 1 of the appendix. The results show good agreement although those labelled STEM 6 (from a chemical defect with a sphere) are slightly anomalous. The nominal composition of chemical defects having spheres (STEM3 and 6) is very comparable to that of defects not having a sphere (STEM 9 and 11). All defects show the composition $Ca_xGa_yGe_zO_{12}$ to be rich in gallium and depleted in germanium relative to the $Ca_3Ga_2Ge_3O_{12}$ matrix since y is greater than two and z is less than three in each case. The calcium content of both matrix and defect seems similar since z approximately equals three. By simply taking an arithmetic average of the x,y, and z parameters an average nominal composition of the chemically inhomogeneous material is found to be $Ca_{3.12}Ga_{3.39}Ge_{1.48}O_{12}$.

VI-B. Chemical Analysis/Discussion

The results just presented are subject to limitations inherent in the experimental and analytical methods used. The average nominal composition $Ca_{3.12}Ga_{3.39}Ge_{1.48}O_{12}$ of the chemically defective regions is a result which must be interpreted accordingly. It is likely that there are compositional variations or gradients even within the chemically defective regions and a nominal composition is of questionable

significance. It is equally likely that detailed high resolution chemical microanalysis would reveal differences in composition between the inhomogeneities with a sphere and those without one. Consequently an average composition is of limited value. In addition it was found that during the chemical analysis experiment the electron probe was subject to small amounts of drift relative to the specimen. Thus there results some uncertainty in the area from which chemical information was obtained despite the efforts of the experimenters to minimize this variable. There arises another uncertainty in the composition of the inhomogeneities since they lie central to the depth of the sample. Chemical information is thus likely to have also been obtained from columns of matrix material between the specimen surface and the defect interface and not uniquely from the chemical defect itself. Most of these shortcomings could be minimized through careful operation of the STEM/EDAX apparatus and selectively choosing the areas to be analyzed.

The assumptions used in the quantitative analysis are also subject to limitations. It is generally accepted that the area under a spectral peak for a certain element is proportional to the amount of that element present, and this assumption is not subject to much debate. The second assumption was that the matrix material was stoichiometric $Ca_3Ga_2Ge_3O_{12}$. This was necessary since the STEM/EDAX instruments had not previously been calibrated with samples of known Ca, Ga, and/or Ge concentration for a more accurate determination of the matrix composition. In fact the instruments were to be calibrated for Ca, Ga, and Ge for future

reference on the basis of the matrix spectra experimentally generated, with the assumption that the spectra came from stoichiometric $Ca_3Ga_2Ge_3O_{12}$.

The third assumption is subject to debate since it is conceivable that the chemically defective garnet regions may not have sixty four cations per unit cell (or eight per formula unit). This assumption that $x+y+z = 8$ was necessary since the ratios of areas under the peaks of spectra from the inhomogeneities did not alone yield unique solutions for the parameters x, y, and z of the defect composition $Ca_xGa_yGe_zO_{12}$. A similar assumption based on garnet electroneutrality (i.e., $2x+3y+4z = 24$) could have been employed. This alternative was not used since local variations from electroneutrality are suspected to be involved in the formation of the chemical inhomogeneities. Likewise no experimental evidence has been found of cation vacancies in the inhomogeneous regions, so the assumption of conservation of cation site occupancy was adopted.

The chemical information obtained shows several significant features despite the fallibility of the analysis. Chemical inhomogeneities with and without spheres are undoubtedly related phenomena as indicated by the similarity in their elemental composition. In addition, both result from interactions among chemical species intrinsic to the CGGG system, i.e. Ca, Ga, and Ge. Although traces of Fe and Cu were consistently detected, they were attributed to the iron pole pieces in the scanning transmission electron microscope and the 3 mm copper grid on which the specimen was mounted. This was verified by the presence of only Fe and Cu peaks in background spectra

recorded while the electron beam was directed through the center of an ion-milled hole in the specimen without impinging on the specimen itself. Consequently the chemical defects seem to result from small scale segregation of gallium in the garnet structure. These micro-segregates, as they may be referred to henceforth, are depleted in germanium, enriched in gallium, and equivalent in calcium content relative to the $Ca_3Ga_2Ge_3O_{12}$ matrix.

A garnet having composition $Ca_{3.12}Ga_{3.39}Ge_{1.48}O_{12}$ would have a larger lattice parameter than $Ca_3Ga_2Ge_3O_{12}$ since garnets obey Vegard's rule[5] and the ionic radius of Ga^{3+} is larger than that of Ge^{4+} by about 0.009Å. The lattice parameter for such a garnet would be on the order of 12.26Å.

To maintain electroneutrality a garnet of composition $Ca_{3.12}Ga_{3.39}Ge_{1.48}O_v$ would need $8x(3.12x2 + 3.39 \times 3 + 1.48x4) = 176$ units of negative charge per unit cell. This could be supplied by only eighty nine O^{2-} ions, and there would be surplus oxygen in a region of such a garnet phase if the normal ninety six oxygens per garnet unit cell are available. This surplus oxygen could be involved in the formation of the oxygen filled sphere, with the accumulation of oxygen motivated by electrostatic imbalance as the crystal cools.

The dark appearance of the microsegregates in both BF and DF is not explicable in terms of the chemical analysis alone. Since gallium has a lower atomic scattering factor than does germanium, the gallium-rich microsegregate region might be expected to appear lighter than the matrix and this is not observed. This indicates that the absorption processes within the segregated regions are dependent

on structural as well as chemical factors and detailed theoretical analysis of constructive and destructive interference phenomena would be needed to correlate the multitude of possible cation distributions among the available sites with the observed dark contrast.

The deficiency of germanium displayed by the microsegregates indicates that defect formation is related to the evaporative loss of germanium reported to have occurred during crystal growth. It is possible that as germanium evaporates, for whatever reason, gallium segregates to occupy their normal octahedral sites as well as the tetrahedral sites vacated by the lost germanium. In fact, gallium is known to preferentially occupy the tetrahedral sites in other garnet systems[5] and it is likely that such sites in CGGG would easily accommodate the Ga^{3+} ions since oxygen packing around tetrahedral sites is less dense than the packing around octahedral sites. Calcium, being the largest cation, cannot fit into octahedral nor tetrahedral interstices and it is not surprising that calcium occupancy of dodecahedral sites is maintained in the microsegregated regions.

Little insight has been gained about the chemical nature of the spheres central to some microsegregates. Since oxgyen is resolvable by very few chemical analysis techniques, the nature of the sphere may have to be deduced in the future rather than established directly. If evaporation of germanium occurs during crystal growth even with an imposed atmosphere of 760 torr oxgyen partial pressure, then segregation of Ge may also be expected around a sphere if it is filled with oxygen gas under pressure. Consequently a germanium concentration gradient may be found to exist in the region of inhomogeneity between the maxtrix/

microsegregate interface and the sphere interface in a microsegregate with an oxygen filled sphere. The higher oxygen pressure of the sphere could attract germanium much as the atmosphere above the growth melt does and germanium concentration near the surface of the sphere may be higher than elsewhere within the microsegregated volume. This type of gradient would have to be established by further high resolution chemical micro-analytical techniques.

Chemical analysis of the defects was originally attempted using a different scanning electron microscope equipped with EDAX. The resolution of that instrument was inadequate to distinquish the composition of the microsegregates from that of the matrix. However, in an effort to expose more of the microsegregated volume in the SEM specimens, they were placed in 250^{o}C phosphoric acid for one hour in order to etch away the matrix material. Stereo analysis of the SEM micrographs showed linear arrays of pits about 0.5μ in size. These pits are of about the same size and distribution as was found for the microsegregates using TEM techniques. Thus it seems that the microsegregate regions were preferentially attacked by the acid. This is significant because it shows that chemical thinning techniques using hot H_3PO_4 (as is used for other garnets) are not viable methods for preparing TEM samples of CGGG for microsegregate analysis.

VII-A. Dislocations/Results

Dislocations in the CGGG samples tended to be in close physical proximity to the microsegregate defects. They were found to always be in the matrix material at or near the defect interface but never internal to the defects. Although isolated matrix dislocation loops such as those reported by Mishra and Thomas[32] were also observed, it can be generalized that the density of dislocations not associated with the chemical defects was low. Dislocation lines and loops were seen but other types such as regular or sheared dislocation helices were not encountered as have been reported in other garnet systems.[34]

The dislocation lines and loops assumed many different geometries, with one example already seen in Fig. 6. Despite this diversity three major types of dislocations were identified. They have been classified as Types 1, 2, and 3 for brevity of later reference to these dislocation configurations, and a description of each type follows. (1) Dislocations specified to be Type 1 can be seen in the regions labelled d of Fig. 10. These are dislocation lines which lie primarily in the matrix material but are in contact with the defect/matrix interface. Such dislocations are usually associated with isolated microsegregates which: (a) are not in a linear array, (b) have developed a central sphere, and (c) tend to have a facetted or crystallographic (rather than curved) sort of interface. The dislocations are inclined to the specimen surfaces and situated at each corner of the defect/matrix interface. Dynamical contrast phenomena have hindered characterization of Type 1 dislocations, however it is certain that these are dislocation lines and not segments of dislocation loops which encircle the

inhomogeneous region. This is true since the dislocations could be made to go out of contrast individually whereas segments of a dislocation loop retain the same Burgers vector and would be expected to disappear simultaneously. No evidence of dissociation into partial dislocations was found. Specimen tilting for $\vec{g}\cdot\vec{b}$ analysis gives agreement with the previously published results of Mishra and Thomas[32] that the Burgers vectors of such Type 1 dislocations lie parallel to <112> crystallographic directions. (2) Type 2 is the designation given to dislocations of the sort seen in region d of Fig. 15A and B. The dislocations are out of contrast in C. These are dislocation lines lying entirely in the matrix region near an isolated microsegregate containing a sphere. Evidence of interactions between the dislocation and the chemically defective region can be seen. The inhomogeneity has a predominantly curved interface although the section of interface nearest the dislocations is seen to have a flat, linear projection oriented almost parallel to the dislocation line direction. The sphere is seen to be displaced from the center of the inhomogeneity so as to be near this flattened interface and the dislocations. The mottled appearance of the background in the micrographs of Fig. 15 is attributed to the carbon film deposited on the specimen surface. Type 2 dislocations are deduced to be of mixed screw and edge character having Burgers vectors parallel to <113> directions which are neither strictly parallel nor perpendicular to the <210> dislocation line directions. They are assumed to be perfect since evidence of dislocation dissociation in weak-beam dark field or high order bright field micrographs has not been found. (3) The third common configuration of dislocations

is illustrated in Fig. 16. A microsegregate with a sphere is imaged in bright field under three different diffracting conditions. Two dislocation loops about 0.5μ in diameter are seen to encircle the defective region in Fig. 16A. The loops are viewed nearly edge-on in a direction parallel to [001]. These loops are mutually perpendicular to each other and extend beyond the defective region at its equator into the matrix material where evidence of strain contrast is faint yet detectable. In the micrographs of Figs. 16B and C the specimen was tilted to make each of these Type 3 loops go out of contrast in turn. Each loop is seen to disappear when the operating diffraction vector $\vec{g}$ lies parallel to the edge-on projection line of the loop. Trace and $\vec{g}\cdot\vec{b}$ analyses reveal such dislocation loops to be of edge type and no evidence of dissociation of the loops into partial dislocations is seen. The Burgers vector for each loop is of magnitude $a_o\langle 100\rangle$ and is directed perpendicular to the {100} plane on which the loop lies.

Another example of Type 3 loops encircling a chemical defect with a sphere is seen in the weak-beam dark field micrograph of Fig. 17. The view is parallel to $[1\bar{2}0]$ and one loop on (001) is seen edge-on while evidence of multiple dislocation images on the mutually perpendicular (010) plane can be seen at d. No evidence of intensity fringes can be seen between the multiple images. The edge-on loop was made to go out of contrast in diffracting conditions consistent with a Burgers vector of $a_o\langle 001\rangle$ perpendicular to the plane of that loop. However during specimen tilting the contrast from the loop or loops giving rise to the double dislocation image did not show

disappearances as anticipated for the expected Burgers vector(s) parallel to [010]. Although the Burgers vectors were not definitively established they are not parallel to <010>. Dynamical contrast phenomena can account for the white blotches of intensity seen in the micrograph of Fig. 17.

The interstitial or vacancy nature of the Type 3 dislocation loops was not ascertained since inside/outside contrast was negligible upon tilting to and from known crystallographic poles.

VII-B. Dislocations/Discussion

The fact that dislocations interact with the microsegregate defects is readily apparent. Chemical forces and strain energy associated with the microsegregates are suspected driving forces for these interactions. The particular defect configuration observed depends not only on the complex chemistry and crystallography of the CGGG system but also on the material processing parameters. The interplay between strain and chemical forces is indicated by the absence of $a_o/2$<111> Burgers vectors. While this is the shortest perfect b.c.c. lattice translation vector it has been theoretically shown[15] to imply strong electrostatic contributions to the defect energy. This accounts for the alternative Burgers vectors experimentally observed to be parallel to <001>, <112>, and <113>.

Dislocations near the microsegregates act to relieve strain due to lattice mismatch between the garnet structures of the matrix and the microsegregates. This is suggested by the fact that all dislocations were found to lie primarily in the matrix and is apparent from the reduced matrix strain contrast associated with dislocated

microsegregates. It is possible that the various types of dislocations were always in the matrix material and were later attracted to the region of the growing chemical inhomogeneity. Under this circumstance it might be expected that matrix dislocations would be seen in the vicinity of the strained chemical defects (not having central spheres) and these are seldom observed experimentally. Instead it is more likely that dislocations are generated by the growing microsegregates. Size of the chemical defect alone is not a critical factor governing dislocation generation since strained chemical defects have been observed in the same area as dimensionally smaller dislocated microsegregates (which also had the internal oxygen filled sphere). Strain energy per unit volume and segregate concentration, which are not completely independent parameters, are more likely to govern dislocation formation.

A correlation between dislocation generation and sphere formation has been alluded to but it is not a straightforward one. While it is true that microsegregates having Type 1, 2, or 3 dislocations were always seen to have the oxygen filled sphere in their interior, it was not uncommon to see microsegregates with spheres which showed no evidence of such dislocations. Consequently it seems that sphere formation and dislocation generation are mutually influential processes. Qualitative evidence of such an influence is seen by the sphere of Fig. 15 being displaced from the center of the microsegregate volume toward the dislocation line in the matrix.

To ascertain the nature of the interaction between a micro-segregate and a Type 1 or Type 2 dislocation line would require atomistic determination of the permutations in lattice positions and consequent

electrostatic and strain energies associated with their respective Burgers vectors of a_o<112> and a_o<113>. This was not accomplished but will be necessary in the future if the role of Type 1 and Type 2 dislocations in microsegregation phenomena in CGGG is to be fully appreciated. Type 1 dislocations are probably generated near the corners of the facetted microsegregates due to stress concentrations in those regions.

The Type 3 dislocation loops of Figs. 16 and 17 are always found to encircle the microsegregates and lie in the matrix material several hundred angstroms away from the interface. This suggests that the dislocation accomodates matrix strain and that while the dislocation may have been generated at the interface it has grown into the matrix by climb. These Type 3 loops lying on {001} planes are seen face-on in region S in the plane of the {001} oriented foil of Fig. 12A and give rise to the split-ring image typical of edge dislocation loops. The line of no contrast perpendicular to the operating $\vec{g}$ occurs since the invisibility criterion $\vec{g}\cdot\vec{b}x\vec{u} = 0$ is satisfied at these locations ($\vec{u}$ = a unit vector tangent to the dislocation loop at any point on the loop).

The double dislocation image of region d of Fig. 17 can be interpreted as follows: (1) a double image of a single dislocation line, (2) one image each of two different concentric loops, or (3) two partial dislocations separated by a region of stacking fault. The result that the loop does not have the usual a_o<001> Burgers vector gives support to alternatives (2) and (3). Alternative Burgers vectors might be expected to make two concentric perfect loops stable

whereas Burgers vectors of $a_o\langle 001\rangle$ may be preferred for the single Type 3 loop configuration. Likewise two concentric partial dislocation loops may be stable due to energy reductions from dissociation of a perfect loop. The perfect loop could have any of a number of Burgers vectors, but for a Type 3 loop with $\vec{b} = a_o\langle 001\rangle$ several dissociations are possible which conserve octahedral cation positions.[15] Future verifications of the perfect or partial nature of these multiple loops and their Burgers vectors will give considerable insight into the elastic and electrostatic energies which govern crystal defects in CGGG.

The possibility that the double dislocation image arises from a single dislocation must not be overlooked. Mishra and Thomas[32] have shown through calculations of theoretical image profiles that double images of a single undissociated dislocation can still arise despite the increased resolution obtained from weak-beam dark field imaging.

Mechanisms for dislocation loop generation around chemical inhomogeneities were proposed by J. W. Matthews[35] as a result of his work on gadolinium gallium garnet. Similar mechanisms have been proposed in metallic systems as well.[36] A mechanism proposed by Matthews to account for the formation of single loops around inclusions requires the formation of a small prismatic loop outside of the inclusion (see Fig. 18A). The loop grows by the addition of point defects as shown in Fig. 18B. This is a misfit dislocation accommodating lattice mismatch between the inclusion and the matrix. However, if the concentration of point defects is very high in the vicinity of the loops, then the growth of the loop may continue via climb until the configuration

of Fig. 18C is reached. The loop remains near the equatorial plane of the inclusion and is stable with respect to glide because of the interaction between the strain fields of the loop and of the inclusion.

Once a single large loop has grown, another concentric loop may form and grow by repeating the same process. This can account for the observation of two concentric and apparently coplanar dislocation loops in Fig. 17. Likewise, the two images could be from a single dislocation formed by the above process which dissociated into partials. Stacking fault fringes might not be seen between the partials if the splitting distance is small and the extinction distance is large (since fringe spacing $t \propto \xi_g$).

A similar mechanism proposed by Matthews to account for multiple loop generation begins with the formation of a small prismatic dislocation loop immediately outside of the inclusion (see "a" of Fig. 19). This loop has its plane normal to both the surface of the inclusion and the Burgers vector of the loop. Growth occurs by absorption of interstitials or emission of vacancies (for an interstitial loop) until a crescent-shaped configuration is achieved (like "b" in Fig. 19). The point defects are activated by the elastic strain energy due to the inclusion. The strained nature of the segregated regions of Fig. 8 supports the viability of this mechanism for the CGGG system.

Continued growth permits portions of the loop to meet on the opposite side of the inclusion where they annihilate leaving a pair of concentric loops c_1 and c_2. Two main forces act on loop c_2 and the relative magnitudes of these forces determines whether a loop like c_2 is glissile. One force is due to the inclusion and tends

to increase any movement of the loop away from the equatorial plane of the inclusion. The other force is due to the misfit dislocation c_1 and tends to return the outer loop to the equatorial plane. Still another force may need to be considered in garnets such as CGGG. The Burgers vectors of perfect dislocations could favor loops c_1 and c_2 having partial Burgers vectors with the loops connected by an area of stacking fault. These stacking faults could hinder motion of the loops away from the equatorial plane. The above discussion could also account for the observation of double dislocation images in Fig. 17.

Both of Matthews' theories were developed for the case of an isotropic material. While the linear arrays of microsegregates indicate anisotropy in CGGG it is possible that the anisotropy will not preclude the operation of either of the above loop formation mechanisms, but rather it may dictate the types and configurations of dislocations which are found.

VIII-A. Coherent Precipitates/Results

Another distinct defect configuration commonly encountered can be seen in Fig. 20. These look like small loops about 0.1μ in size and are not physically associated with established microsegregate defects as are dislocation Types 1, 2 and 3. Contrast from the interior of such loops is not clear but it sometimes appears that a fringe or some other feature may be present in some. The matrix material has a pocked appearance suggestive of the presence of point defects. The density and distribution of the pocked appearance and the small loops was unaffected by long exposure (several hours) to an intensely focussed beam of 650 kV electrons. Several general observations were made concerning the distribution of the small loop-like features. (1) They were not distributed homogeneously throughout the bulk of the samples. Where the density of the larger microsegregates was very high, the density of these small loops and point defects was low or zero. (2) Where the small loops were observed they were seen in great numbers and found to always show evidence of pocked background.

Contrast from these loop-like features was very sensitive to diffracting conditions such as the particular operating reflection excited and the deviation parameter s. Image quality was improved using s slightly positive as determined in the diffraction mode by the Kikuchi line outside of the operating diffraction spot. Stereomicroscopy showed these loops to be distributed fairly uniformly throughout the thickness of the specimen whereas the pocked appearance seemed to be localized near the surfaces. Loops seemingly near the specimen

surface often displayed anomalously wide images (see Fig. 21) which could not be improved with high-resolution BF or DF imaging techniques.

Selected area diffraction patterns from the areas of the sample where the small loops were profilic did not contain extra spots, streaks, or other anomalies not resolved in S.A.D. patterns obtained from undefective CGGG matrix.

Despite meticulous tilting of the specimen the small loops could not be made to go out of contrast completely. Loops viewed face-on commonly show a line of no contrast through the loop in a direction perpendicular to the operating diffraction vector $\vec{g}$ (Fig. 22). Stereographic analysis of face-on and edge-on loops in the [001] oriented specimen of Fig. 22 showed the loops to be lying on {001} type planes, however similar analysis of other loops indicated that alternative habit planes are also likely. Systematic tilting of the specimen failed to reveal a consistent scheme of inside/outside contrast for determining intrinsic or extrinsic nature of the loops.

Several of the small loops can be seen in very close proximity to each other in region C of Fig. 20. The identity of the individual loops has been obscured in the region where their images overlap. Stereomicroscopy of these loops indicates that coalescence of the disc-like loops into a three-dimensional feature has occurred as opposed to merely appearing to overlap in the projected image. Evidence of such coalescence of small loops was not uncommon.

The pocked appearance of the matrix around the small loops displays several contrast effects. The small "points" are observed to reverse contrast across an extinction contour in Fig. 21.

In addition, the BF/DF pair of Fig. 20 shows the points to have a black-white lobe contrast. The direction $\vec{q}$ of white to black contrast is seen aligned both parallel and antiparallel to the operating diffraction vector $\vec{g}$, depending on the particular point under consideration. Furthermore, examples of the line of black to white contrast being either identical or reversed for a particular point in a BF/DF pair can be found. These types of contrast behavior are usually attributed to point defect clusters in the specimen[37], with contrast being governed by the diffracting conditions, the interstitial or vacancy nature of the defects, and their depth distribution in the foil.

VIII-B. Coherent Precipitates/Discussion

Contrast from the small loop-like features indicates that they may be either dislocation loops or else coherent or partially coherent precipitates. Distinguishing between these various possible defects is sometimes difficult on the basis of contrast phenomena alone. Other workers[38] have been able to differentiate these features by mechanically and thermally treating their specimens and determining whether the observed microstructural changes and properties correlate more closely with dislocation or precipitate behavior. Such thermo-mechanical treatments were not performed on the CGGG samples. However, qualitatively it is easier to explain formation of three-dimensional defects in terms of coalescence of precipitates rather than dislocations. Also, prismatic loops might be expected to show very weak or zero contrast in some diffracting conditions where $\vec{g}\cdot\vec{b}=0$, and no reflection was found which caused virtual disappearance of any of these features. Additional evidence will be presented later to support the notion

that these are small disc shaped precipitates. Consequently it is assumed that they may be coherent or partially coherent precipitates since these can each theoretically give rise to contrast similar to that observed experimentally. Partially coherent precipitates commonly show interfacial misfit dislocations but evidence of such dislocations was not found. Furthermore it is reasoned that the precipitates are likely to be coherent since partially coherent precipitates often have a structure different from the matrix and give rise to extra spots in the diffraction pattern which are unique to the precipitate. Such extra spots were never isolated using DF methods and therefore the loops are attributed to 0.1μ diameter disc-shaped coherent precipitates.

A coherent precipitate can give rise to contrast very similar to a prismatic dislocation loop of partial "Burgers vector" $\vec{b}_p$ provided that the strains in the plane of the disc are very small and the major displacements of magnitude $|\vec{b}_p|$ occur in directions perpendicular to the plane of the disc. When such a disc is viewed face-on, the experimentally observed line of no contrast will be seen at points where $\vec{g}\cdot\vec{b}_p x\vec{u}=0$, where $\vec{u}$ is a unit vector tangent to the edge of the disc at any point. Since $\vec{b}_p$ is normal to the plane of the disc and $\vec{u}$ lies in it, $\vec{g}\cdot\vec{b}_p x\vec{u}=0$ only when $\vec{u}$ lies parallel to $\vec{g}$ and a line of no contrast is seen perpendicular to $\vec{g}$ (where $\vec{g}$ and $\vec{u}$ are parallel). Such a line of no contrast perpendicular to $\vec{g}$ can be seen in Fig. 22.

Wide images such as those of Fig. 21 have been observed from coherent precipitates in other systems as well.[27] These are generally attributed to surface relaxation effects of strain fields from precipitates lying within half an extinction distance of the foil surface.

The thickness of the discs as established by measurement of the minimum image width of edge-on precipitates tended to be on the order of a few hundred angstroms. Dynamical contrast from the precipitates has hindered a more specific determination. It is doubtful that the precipitates are substantially thinner than this since streaking in the diffraction patterns along directions normal to the projected images of edge-on discs would be expected but was not observed experimentally.

Several factors indicate that the small loop-like precipitates are related to the larger microsegregate defects. Specimens often contained both types of defects except in different areas which were usually separated by regions of undefective matrix. Both types of defects are observed in the bulk of the specimens suggesting that they are defects intrinsic to CGGG and not just specimen preparation artifacts. The {100} habit plane of the small precipitates is reminiscent of the {100} habit plane of the large edge dislocation loops surrounding the microsegregates with spheres. These precipitates could conceivably act as nucleation sites for the small climb loops of Matthews' theory.[35] In addition, the observed coalescence of several precipitates into a three dimensional mass indicates that the precipitates are a preliminary stage in the formation of the larger microsegregate defects. The three dimensional microsegregate morphology is obtained from the two dimensional disc-shaped precipitates since they are randomly distributed on the three mutually perpendicualar {100} cube faces in the lattice.

Chemical analysis was performed on the small precipitates in an effort to correlate their composition with that of the larger microsegregates. An analysis was conducted using STEM/EDAX by placing a 200Å diameter probe of 120 keV electrons central to a face-on precipitate for a specific counting time and comparing the chemical information thus obtained with information gotten by the same methods from undefective CGGG matrix regions. Representative STEM/EDAX microanalysis spectra are shown in Fig. 23. Two major conclusions can be made as follows: (1) the precipitates show no evidence of elements extrinsic to the CGGG system (except Fe and Cu as explained previously), and (2) the composition of the precipitate shows negligible difference from that of the matrix. Consequently the precipitates are not due to inclusion of elements extrinsic to the CGGG sample, such as platinum from the crystal growth crucible.

It is likely that careful re-execution of this experiment will reveal the precipitates to be rich in gallium and depleted in germanium as would be expected for the coalescence model of microsegregate formation. The reasons for not verifying this in the original chemical analysis are three-fold: (1) The specimens used for the analysis were thick relative to the thickness of the small precipitates. Consequently substantial amounts of matrix material would be found in columns above and below the precipitates and the chemical information from this matrix material masks the information obtained from the precipitate. (2) The STEM instrument was subject to instabilities which make the probe move relative to the target (or vice versa) by distances on the order of 500Å. Thus there is a finite probability that chemical information

was being received from areas other than the original precipitate target area despite the best efforts of the experimenters to eliminate this source of error. (3) No high resolution chemical analysis apparatus was available at U.C. Berkeley or Lawrence Berkeley Laboratory necessitating travel to Rockwell Science Center where access to such equipment was limited in duration.

Stereomicroscopy has shown that the features giving rise to the pocked appearance of the matrix tend to be localized near each of the specimen surfaces. The various contrast phenomena observed, i.e., the line of black to white contrast, the identical or complementary nature of contrast in DF/BF pairs, and the reversal of contrast across an extinction contour, are consistent with contrast from point defects or clusters located near both surfaces of the specimen. If these point defects are not homogeneously distributed in the thickness of the specimen they are probably not defects intrinsic to CGGG. They are not likely to arise due to irradiation in the electron microscope because their density would be expected to change while under the influence of the electron beam and they should be preferentially located near only the top surface of the foil where the electron beam impinges. Therefore they are expected to arise from two-sided ion milling of the samples which accounts for their distribution near both surfaces of the TEM specimens. The strain energy from the precipitates contributes to the process of cluster formation, making the area adjacent to such precipitates more susceptible to ion damage. Controlled ion thinning experiments could be done in the future to confirm the origin of such defects in CGGG.

The possibility that these clusters are intrinsic to CGGG and exist in the bulk of the specimens cannot be precluded because of the thickness of the samples used. Ascertaining the depth distribution of these clusters was hindered by the mottled contrast expected from such clusters if they are located near the center of a specimen which is several extinction distances thick. Such clusters in the bulk could be involved in precipitate and microsegregate formation. The density of the clusters would then be expected to be low in the vicinity of large microsegregates (as is observed experimentally) since the clusters could be consumed during precipitate formation and subsequent growth into larger microsegregates.

IX. Model for Microstructure Formation

The results and discussion presented suggest a model of microsegregate defect formation which entails nucleation and successive stages of growth of the chemically inhomogeneous regions. The multiplicity of observed defect configurations is too great to allow a general theory accounting for all of them. Consequently this model is concerned only with the formation of a microsegregate defect having a central oxygen-filled sphere and encircled by a single undissociated Type 3 dislocation loop.

Defect formation commences with the random nucleation of the small loop-like precipitates shown in Figs. 20-22. This occurs due to the preferential evaporative loss of Ge from the melt and results in local deviations from stoichiometry. Evaporation rate is sensitive to temperature[9] (and oxygen partial pressure) and consequently thermal fluctuations in the melt solution can be responsible for localized germanium loss. As the germanium is lost through evaporation the small loop-like second garnet phase is formed by incorporating Ga^{3+} ions in sites of the growing crystal which would normally be occupied by Ge^{4+} ions.

Random nucleation continues due to loss of Ge from the melt and is followed by growth of the coherent loop-like precipitates which generate strain. As growth procedes the strain fields of neighboring particles start to overlap. Continued growth and interaction of overlapping strain fields then enhance coalescence of closely spaced individual precipitates into a larger chemical defect, as is indicated in region C of Fig. 20. The result of such coalescence of small

loop-like precipitates is the larger strained chemically inhomogeneous regions (without the central sphere) as is seen in Figs. 8, 11 and 12.

Coalescence of small precipitates into the larger, strained chemical defects continues until the population of the larger defects is great enough and their physical separation small enough to permit interaction of overlapping strain fields. Strain field interactions then motivate the alignment of the defects along crystallographically soft directions as dictated by the anisotropic elastic constants of the material. This notion of formation of larger chemical defects from the coalesence of smaller loop-like precipitates and their subsequent alignment due to strain is consistent with the observations of Fig. 24. The bright field micrograph of an [001] oriented CGGG specimen shows the larger chemical inhomogeneities (some with evidence of the internal sphere) aligned along [100] amidst a proponderance of the randomly distributed small loop-like precipitates. The region of material on either side of the linear array is depleted of the small precipitates. Such a denuded band around the larger defects verifies their formation by coalesence of the small loops.[28]

Evidence supporting the succession of events up until this stage of defect formation has been gained through HVEM. However the material factors and chronological succession of events leading to further formation of the internal oxygen filled sphere and/or encircling dislocation loop has not been ascertained. It is probable that both processes occur upon cooling the crystal and proceed as follows. Formation of a single dislocation loop could occur by the method of Matthews[34] as shown in Fig. 18. This method requires formation of a small

prismatic loop outside of the microsegregate. Such small prismatic loops have been observed to nucleate around small precipitates in other systems[36,39] and the small loop-like precipitates found in CGGG are suspected to act as nucleation sites. The loop is nucleated due to strain which is enhanced upon cooling and grows to successively larger diameters (Fig. 18B and C) by climb. Point defects (vacancies or interstitials) are absorbed or emitted by such a climb loop during growth until it reaches the equatorial position around the microsegregate where strain energy stabilizes it with respect to glide. The observed evidence of point defects in CGGG suggests that they arise due to ion milling and would consequently not be involved in loop formation. To verify the mechanism of loop formation in CGGG would require determining the interstitial or vacancy nature of the loop as well as further characterization of the type, distribution, and origin of the point defects in CGGG. Size of the microsegregate defect does not seem to be the only critical factor in loop formation since relatively large (0.6μ) as well as small (0.2μ) microsegregates have been observed with and without encircling loops. Instead strain energy per unit volume is suspected as a critical factor since it is independent of size.

Generation of the mutually perpendicular Type 3 loops seen in Fig. 16A requires only that the individual loops nucleate around small precipitates lying on mutually perpendicular {100} planes. Three mutually perpendicular loops on {100} could conceivably encircle a microsegregate. This is not observed experimentally since one of the <100> was coincident with the crystal pulling/rotation axis during

growth of the CGGG boule. Thus during processing the <100> pulling direction was the zone axis for two equivalent {010} (on which loops form) whereas the remaining {100}, whose normal was the pulling axis, was different.

Formation of the oxygen-filled sphere is likely to accompany or follow relief of microsegregate strain since microsegregates with the central sphere seldom show pronounced strain contrast. The oxygen within the sphere can be supplied by the constituent garnet oxides of the melt or the imposed oxygen partial pressure of 760 torr above the melt solution. Since the size of the sphere is always observed to be proportional to the size of the microsegregate in which it is found (i.e., the diameter of the sphere is always about one third of the largest dimension of the microsegregate) the oxygen is probably supplied from the melt solution in the following manner. The evaporation of Ge permits accomodation of Ga^{3+} ions on tetrahedral sites of the growing crystal normally occupied by Ge^{4+} ions. This substitution results in a metastable phase at the growth temperature since the size of Ge^{4+} and Ga^{3+} ions do not vary greatly and hence small strains are involved. The metastable nature of these regions is indicated by the preferential etching of the microsegregates by hot acid. In the regions where Ga^{3+} has been substituted for Ge^{4+} there would be a deficiency of positive charge. This can be remedied by supplying additional positive charges or eliminating some negative charge. Supplying positive charge is not feasible since this is most easily accomplished using the Ge^{4+} ions which evaporate. Instead negative charges are deleted by the leaching out of O^{2-} anions as the crystal

cools. Since the matrix surrounding the microsegregate defect is stoichiometric $Ca_3Ga_2Ge_3O_{12}$ with the proper amount of oxygen, the O^{2-} anions diffuse away from the matrix, i.e., toward the center of the microsegregate. Accumulation of these anions occurs to form the oxygen filled sphere whose shape is maintained by the pressure of the accumulated oxygen gas.

From this model it is suggested that defect formation could depend upon evaporative loss of Ge from the melt. Thermal conditions in the melt solution and growth atmosphere have been shown to influence the rate of loss of Ge.[9] Consequently any effort to eliminate the microsegregate defects must address these factors. Specifically, germanium loss due to evaporation may be reduced by imposing a higher GeO partial pressure above the melt (instead of O_2). The vapor pressure of Ge and GeO_2 above their pure substances near the CGGG crystal growth temperature are on the order of 10^{-3} torr. However, GeO is a substantially more volatile component with vapor pressures exceeding 760 torr at 1000°C.[40] Thus germanium loss from the melt may be due to the volatility of GeO at high temperatures and imposing a GeO atmosphere above the melt may reduce the rate of germanium loss. The deposition of GeO_2 on the crystal pulling shaft[9] results by reaction of GeO gas upon cooling in the imposed oxygen atmosphere.

Thermal fluctuations within the melt would be minimized by controlling heat loss from the crucible as well as by insuring that unstable convective currents in the growth melt solution due to specimen wobble during rotation are eliminated.

Conclusions

Several conclusions are apparent as a result of this electron microscopy study of calcium gallium germanium garnet.

(1) High voltage transmission electron microscopy and the techniques of weak-beam dark field and high order bright field imaging have permitted characterization of microsegregate defects and dislocations in CGGG.

(2) Lattice defects observed in CGGG are governed by the complex structure and chemistry of the garnet system. Such defects are of sufficient size and density that they could be detrimental in certain applications in which CGGG single crystals could be valuable, i.e., magnetic bubble memories.

(3) The formation of microsegregate defects is correlated with germanium loss from the crystal growth melt. Evaporative loss of germanium and subsequent microsegregation phenomena may be reduced by properly altering processing parameters. Imposing a higher GeO partial pressure above the melt and eliminating temperature fluctuations in the melt are suggested.

Suggestions for Further Study

Additional work can be performed in the following areas to further this characterization of CGGG defects.

Ion thinning of TEM specimens must be done systematically to determine if the observed point defects are truly specimen preparation artifacts. Techniques for producing thin and uncontaminated CGGG samples suitable for lattice imaging should be developed.

HVEM studies of dislocations and possible dissociations should be pursued using weak-beam DF and high order BF imaging. Such studies could provide insight into the structural and electronic interactions associated with CGGG defects.

Lattice imaging studies of microsegregate/matrix interfaces can establish aspects of coherency, orientation, and possibly compositional fluctuations.

Chemical analysis using high resolution STEM/EDAX to establish local chemical gradients and fluctuations within the bulk of the crystal as well as within individual microsegregate defects will provide further detail for the model of defect formation and suggest dependences on processing parameters.

Heat treatment near the CGGG melting point in an appropriate atmosphere after crystal growth may prove beneficial in suppressing microsegregate and/or dislocation formation and growth.

Acknowledgements

It is a privilege to acknowledge Professor Gareth Thomas for the guidance, encouragement, and opportunities he has provided throughout the duration of this study. I also wish to thank Professor Jack Washburn and Professor Dennis W. Hess for their critical appraisals of the manuscript.

To Dr. Raja K. Mishra goes my most sincere appreciation for the invaluable time, effort, and friendship which he has invested to better my understanding of Materials Science and life in general.

Special thanks go to Dr. David R. Clarke for his collaboration on the chemical analysis portion of this paper as well as the use of the STEM/EDAX facility at Rockwell Science Center in Thousand Oaks, California.

I am greatful for the assistance provided by the Lawrence Berkeley Laboratory staff during the various stages of this study. I wish to specifically thank Don Jurica and Carolyn Gosnell for their diligence in maintaining the TEM lab in working order, Gloria Pelatowski for her flawless reproduction of the line drawings, and all the Photo Lab staff for their punctuality in providing high quality work.

Heartfelt gratitude is extended to my immediate family and my financee Marita Schad for the enduring support and encouragement which only they could provide.

Finally I want to acknowledge J. P. M. Damen and J. A. Pistorius of Philips Laboratories for supplying the material samples used in this study.

This research was performed under the auspices of the United States Department of Energy through the Materials and Molecular Division of the Lawrence Berkeley Laboratory.

Appendix: Chemical Analysis

Chemical analysis was performed at Rockwell Science Center, Thousand Oaks, California using a Philips electron microscope equipped with an x-ray microanalyzer. Chemical spectra from CGGG samples were obtained using a 200Å diameter probe of 120keV electrons. The spectra thus obtained were recorded on computer printout as well as Polaroid photos of a CRT display. The area under a peak of the spectrum for a particular element is assumed to be proportional to the number of atoms of that element present in the area subjected to the electron beam.

Using the technique described above and the analysis which follows, four microsegregate defects (of about 0.4μ size) were investigated and found to have the following compositions.

TABLE 1

Run #	Description	Composition $Ca_xGa_yGe_zO_{12}$ x	y	x
STEM 3	Microsegregate with internal sphere	3.1452	3.8278	1.02711
STEM 6	Another microsegregate with internal sphere	2.965	2.9185	2.1163
STEM 9	Microsegregate without a sphere	3.2009	3.7047	1.0944
STEM 11	Another microsegregate without a sphere	3.1498	3.1257	1.6675

These results were generated from the following tabulated data which show measurements of spectral peak heights, widths at half maximum above background, and calculated areas under the peaks. STEM 1, 5, and 10 are from CGGG matrix regions located about 1μ from the chemical defects of STEM 3, 6, and 11 respectively.

TABLE 2. Matrix Analysis Data

Run #	K_α Peak for	Height	Width	Area
STEM 1	Ca	2790	0.152	212.04
	Ga	1351	0.196	132.35
	Ge	1840	0.208	191.36
STEM 5	Ca	748	0.146	54.6
	Ga	360.5	0.188	33.89
	Ge	469	0.194	45.493
STEM 10	Ca	1047.5	0.143	74.9
	Ga	552.5	0.179	49.45
	Ge	759	0.189	71.72

TABLE 3. Microsegregate Analysis Data

Run #	K_α Peak for	Height	Width	Area
STEM 3	Ca	1712.5	0.144	123.3
	Ga	1479	0.190	140.5
	Ge	395	0.184	36.34
STEM 6	Ca	309	0.135	20.86
	Ga	202	0.199	20.099
	Ge	146	0.184	13.432
STEM 9	Ca	1824.5	0.146	133.19
	Ga	1562	0.188	146.83
	Ge	418.5	0.195	40.8
STEM 11	Ca	1599	0.153	122.32
	Ga	1226.5	0.196	120.2
	Ge	675	0.190	64.125

The following is an illustrative calculation of the composition of the microsegregate of STEM 3. To determine this composition required a calibration of the microscope using the matrix spectra of STEM 1. Since the matrix is assumed to be stoichiometric $Ca_3Ga_2Ge_3O_{12}$, then the ratio of atomic fractions of Ca to Ga in the matrix area of STEM 1 is 3/2, whereas the ratio of Ge to Ga is also 3/2 while the Ca/Ge ratio is 3/3 = 1. However the ratios of areas under the Ca,

Ge, and Ge peaks of STEM 1 shows

(Ca area/Ge area) = 212.04/132.35 = 1.6021

(Ge area/Ga area) = 101.36/132.35 = 1.4459

(Ca area/Ge area) = 212.04/191.36 = 1.1081.

Therefore the actual ratio of areas under the peaks is related to the atomic fraction ratios by

$Ca/Ge = 3/2 = K_1(1.6021)$ $\qquad K_1 = 0.9363$

$Ge/Ga = 3/2 = K_2(1.4459)$ $\qquad K_2 = 1.0374$

$Ca/Ge = 3/3 = K_3(1.1081)$ $\qquad K_3 = 0.90245$

where K_1, K_2, and K_3 are lumped constants which account for such factors as the variability of the STEM/EDAX detector in identifying elements of different atomic number. These constants effectively calibrate the microscope detector since using this information the composition $Ca_xGa_yGe_zO_{12}$ of the microsegregated region of STEM 3 can be deduced. Therefore the ratios of areas under the STEM 3 peaks are:

$Ca/Ga = x/y = K_1(123.2/140.5) = K_1(0.87758) = 0.9363(0.87758) = 0.821652$

$Ge/Ga = z/y = K_2(36.34/140.5) = K_2(0.25865) = 1.0374(0.25865) = 0.26833$

$Ca/Ge = x/z = K_3(123.2/36.34) = K_3(3.39296) = 0.90245(3.39296) = 3.06198.$

However these ratios of the composition parameters x, y, and z alone do not yield a single convergent solution to the composition. Therefore an assumption must be made and it is assumed that cation sites in the defective garnet regions are conserved so that $x + y + z = 8$. Since

$$x = 0.821652y$$

and

$z = 0.26833y$ then by solving $x + y + z = 8$

it is seen that

$y = 3.8278$

$z = 1.02711$

and

$x = 3.1452.$

These are the values of the composition parameters found in Table 1 for STEM 3. The values for STEM 6, 9, and 11 are found by similar methods. A nominal composition for a general microsegregated volume was calculated by taking an arithmetic average of the x, y, and z parameters of Table 1. Thus the nominal composition of $Ca_{3.12}Ga_{3.39}Ge_{1.48}O_{12}$ were derived.

References

1. T. H. O'Dell, Magnetic Bubbles, John Wiley and Sons, New York, 1974.
2. A. H. Bobeck, P. I. Bonyhard, and J. E. Geusic, Proc. IEEE, 63, #8, 1975, 1176-1206.
3. P. Chaudhari, et al., Physics of Thin Films, 1977, 263-297.
4. E. A. Giess, et. al., Mat. Res. Bull., 8, 1973, 1061-1066.
5. J. E. Davies, and E. A. Giess, J. of Mat. Sci., 10, 1975, 2156-2170.
6. W. L. Roth, from The Chemistry of Extended Defects in Non-Metallic Solids, North-Holland Publishing Co., London, 455-485.
7. M. J. Stowell, from Epitaxial Growth, Part B, Academic Press, New York, 1975, 382-489.
8. J. W. Matthews, et. al., Phys. Stat. Sol (a), 19, 1973, 671.
9. J. P. M. Damen, et al., Mat. Res. Bull., 12, 1977, 73-78.
10. ASTM X-Ray Powder File Index Card #11-23.
11. K. J. Standley, Oxide Magnetic Materials, 2nd Ed., Oxford University Press, 1972, 30-36.
12. R. W. G. Wykoff, Crystal Structures, Vol. 3 Interscience Publishers, Inc., New York, 1960, Chapt. XII, 3-5.
13. S. Geller and M. A. Gilleo, Phys. Chem. Sol., 3, 30, 1956.
14. J. Friedel, Dislocations, Pergamon Press, 1964, 149-160.
15. J. Rabier, P. Veyssiere, and J. Grilhe, Phys. Stat. Sol., (a), 35, 1976, 259.
16. J. P. M. Damen, and J. A. Pistorius, Private communication to Dr. R. K. Mishra, May, 1977.

17. G. Thomas, Proc. 4th Int. Conf. on HVEM, Toulouse, France, 1975, p. 247.

18. R. Osiecki, and G. Thomas, 29th Ann. Proc. EMSA, Boston, Mass., 1971.

19. G. Thomas and M Goringe, Transmission Electron Microscopy of Materials, to be published, J. Wiley and Sons, New York, 1979.

20. D. J. H. Cockayne, J. De Physique, C7, 35, #12, December, 1974, p. 141.

21. J. W. Edington, Practical Electron Microscopy in Material Science, Monograph #3, MacMillan, 1975.

22. J. Rabier, H. Garem, and P. Veyssiere, J. Appl. Phys., 47, #11, 4755-58.

23. B. Hardiman, et. al., Phil. Mag., 27, 1973, 777.

24. International Tables for X-Ray Crystallography, Vol. 1, The Kynoch Press, Birmingham, England, 1952, pgs. 55, 345-346, 524-525.

25. J. W. Edington, Practical Electron Microscopy in Material Science, Monograph #2, MacMillian, 1975, 59-62.

26. K. N. Tu and A. Howie, Phil. Mag., B, 37. #1, 1978, 73-81.

27. P. B. Hirsch, et. al., Electron Microscopy of Thin Crystals, Butterworths, 1965, 96-97, 328-332.

28. H. F. Merrick, and R. B. Nicholson, 5th Int. Cong. for Electron Micros., Vol. 1, K8, Academic Press, N. Y., 1962.

29. F. R. N. Nabarro, Proc. Phys. Soc., 52, 1940, 90; Proc. Roy. Soc., A175, 1940, 519.

30. J. W. Cahn, from The Mechanisms of Phase Transformations in Crystalline Solids, Inst. of Metals, London, 1969, 1.

31. Landolt-Bornstein Tables, New Series, Group III, Vol. 1, p 10, 31, and Vol. 2, p 6-7, Springer-Verlay, New York, 1966.

32. R. K. Mishra and G. Thomas, J. Appl. Phys., 49, #3, March 1978, 1876-1878.

33. J. I. Goldstein, J. L. Costley, G. W. Lorimer, and S. J. B. Reed, Scanning Electron Microscopy/1977, 1, 315-24.

34. J. W. Matthews, et. al., Phys. Stat. Sol. (a), 28, 1975, 95-105.

35. J. W. Matthews, Phys. Stat. Sol., (a), 15, 1973, 607.

36. A. Eikum and G. Thomas, Acta. Met., 12, May 19¢4, 537-545.

37. M. Wilkens, from Modern Diffraction and Imaging Techniques in Material Science, Ed. S. Amelinckx, et. al., North-Holland Publishing Co., 1970, 233-256.

38. D. Hull and I. J. Mogford, Phil. Mag., 6, 1961, 535.

39. K. H. Westmacott, et. al., Phil. Mag., 7, 1962, 1585.

40. Davydov, V. I., Germanium, Gordon and Breach Science Publishers, New York, 1966, p. 144-187.

Figure Captions

Fig. 1. A) Garnet dodecahedral or c sites have the least dense packing of oxygen and are occupied by the largest cations, Ca^{2+} in CGGG. An oxygen ion is located at each of the eight vertices of the dodecahedron with the cation central to its interior. There are three c sites per garnet formula unit.

B) Octahedral cation sites are surrounded by six closely packed oxygen ions and are usually occupied by the smallest cations. There are two octahedral (or "a") sites per chemical formula unit.

C) Tetrahedral coordination of oxygen provides d cation sites of size intermediate between the a and c sites in garnets. There are three such sites per formula unit and in CGGG these sites must be at least partially occupied by the smallest (Ge^{4+}) ions.

Fig. 2. The cations are arranged in one octant of the unit cell such that the oxygen polyhedra share edges and vertices. Each oxygen is shared by one tetrahedral, one octahedral, and two dodecahedral sites (one of which has been eliminated in the figure for clarity).

Fig. 3. A) Each octant of the unit cell contains one garnet formula unit. The octahedral or a sites are distributed with body centered cubic symmetry in each octant.

B) The distribution of tetra- and dodecahedral sites is along the non-diagonal cube face bisectors of each octant.

C) The c and d sites are distributed alternately along the mutually perpendicular face bisectors so as to define a three-fold axis along <111>.

Fig. 4. A) The entire unit cell can be generated from a single octant by considering the non-diagonal face bisectors to be two-fold axes of rotation.

B) By successively rotating the octant cube by 180° about these axes the partial unit cell can be generated having <111> axes distributed as shown.

C) Continued rotation of 180° about the octant face bisectors generates the garnet unit cell which has a single unique three-fold axis along <111>.

Fig. 5. A) A displacement of $\vec{R}_a = a_o/2\langle 100\rangle$ results in exchanging tetrahedral and dodecahedral sites whereas the densely packed b.c.c. octahedral sublattice is unaltered.

B) A displacement of $\vec{R}_b = a_o/2\langle 110\rangle$ produces similar results to $a_o/2\langle 100\rangle$. Consequently defects in garnets producing these displacements have electrostatic as well as elastic energies due to the exchange of cation positions.

C) Displacements of $\vec{R}_c = a_o/4\langle 111\rangle$ leave garnet octahedral sites conserved but alter the distribution of tetrahedral and dodecahedral sites so that formerly unfilled positions become occupied. This results in quite different elastic and electrostatic energies associated with defects producing $a_o/4\langle 111\rangle$ displacements.

Fig. 6. The increased resolution of dislocations in CGGG using high order bright field and weak-beam dark field imaging techniques is seen in A and C respectively as compared with the conventional bright field micrograph of B. The diffraction conditions used are inset in each. Improved resolution of HOBF and WBDF images is invaluable in simplifying the interpretation of contrast from defects in CGGG.

Fig. 7. A) A symmetric [001] diffraction pattern from CGGG shows the existence of {200} as well as {400} type reflections. B) and C) Upon tilting the crystal to excite either of the two mutually perpendicular systematic rows of n{400} (n = an integer) reflections the n{200} reflections disappear. This is consistent with double diffraction phenomena and can be explained in terms of interactions between {400} and {420} reflections.

Fig. 8. Two closely spaced chemical defects about 0.25μ in size are seen as dark oval areas against a lighter CGGG matrix in these BF images. In the sequence ABCD the specimen was tilted to make the diffraction vector $\vec{g}$ rotate clockwise. The lobed contrast distorts to "follow" the operating reflection in a manner typical of strain contrast. Qualitative analysis of these strain effects, accounting for the overlap of strain fields from the two closely spaced defects, shows these are each ellipsoidal in shape.

Fig. 9. Microsegregate defects in CGGG are commonly 0.2-0.6μ in size and consist of a dark halo surrounding a light circular patch. The defect/matrix interface is quite sharp and appears curved in this bright field image.

Fig. 10. A microsegregate in a thin area of a CGGG specimen is imaged in bright field. The light central patch is seen to intersect the specimen surfaces leaving the inner annulus S, and reaches its widest equatorial dimension at M near the middle of the foil. This is consistent with this feature being spherical in shape. Since the electron beam is transmitted undeviated through the inner annulus S, the sphere is believed to be hollow with its spherical morphology maintained by the hydrostatic pressure of oxygen gas. Type 1 dislocations are seen in contact with the interface at the regions designated d.

Fig. 11. The chemical defects both with and without central spheres appear as dark areas against a lighter matrix in both bright field and dark field, as seen in A and B respectively. This indicates that electrons undergo greater absorption in these areas and can be attributed to variations in composition and occupancy of garnet cation sites.

Fig. 12. Microsegregates with and without central spheres are commonly interspersed in linear arrays along <100> directions as seen in this pair of bright field micrographs from adjacent areas in a [001] oriented specimen. Note the split dislocation ring contrast of region S in Fig. 12A having a line of no

contrast perpendicular to $\vec{g}$. The region L of Fig. 12B shows strain field overlap among defects not having developed central spheres. The features marked K are cracks.

Fig. 13. STEM/EDAX spectra showed the segregated regions to be rich in gallium and depleted in germanium relative to the CGGG matrix. This schematically shows that the spectra were obtained by first placing a 200Å diameter probe in the matrix near a defect and comparing the spectrum generated with another obtained by placing the probe on the segregated region.

Fig. 14. Actual spectra obtained from matrix and defect are seen in A and B respectively. The K_α peaks are marked and show that only elements intrinsic to $Ca_3Ga_2Ge_3O_{12}$ were found, except for Fe and Cu which arise from the iron pole pieces of the microscope and copper grid upon which the specimen was mounted. Oxygen was not detectable using this technique.

Fig. 15. Type 2 dislocation lines lying in the matrix of a <120> oriented specimen are seen in region d of the bright field images of A and B. The dislocations are out of contrast in C. These dislocations are mixed in nature having Burgers vectors parallel to [113] and line direction of [210].

Fig. 16. A microsegregate with a sphere in a [001] oriented CGGG specimen is imaged in three different diffracting conditions. In A, two mutually perpendicular Type 3 dislocation loops are seen to surround the segregate while in each of B and C the crystal was tilted to make each of the loops go out

of contrast in turn. Trace and $\vec{g} \cdot \vec{b}$ analyses show these loops to be of edge type having Burgers vectors along the <100> directions normal to the {100} planes on which the loops lie. Notice that the loops extend beyond the segregated region and into the matrix material indicating that climb has occurred. The feature K is a crack.

Fig. 17. In this WBDF micrograph an isolated segregate in a <120> oriented specimen has been imaged and the spherical void and dislocation loops on {100} planes are visible. Note the two dislocation loop images in the region marked d. It is suspected that this is not a double image of a single loop because of the weak beam conditions used to form the image. Instead this is evidence of either two concentric and coplanar perfect dislocation loops or a single dislocation loop which has dissociated into partials lying on a {100} plane.

Fig. 18. A mechanism proposed by Matthews for growth of single (or multiple) large loops around inclusions in gadolinium gallium garnet reguires a small prismatic loop outside the inclusion to grow by climb according to the sequence seen in A, B, and C.

Fig. 19. Matthews mechanism for formation of pairs of loops around chemical inhomogeneities calls for a small prismatic loop "a" to be nucleated. It grows by absorbing point defects until the configuration b is reached. Continued climb permits the crescent shaped loop to encircle the inclusion until

intersecting sections annihilate upon contact on the other side of the inclusion, leaving two concentric loops C_1 and C_2 having the same Burgers vectors.

Fig. 20. Small loop-like precipitates 0.1μ or less in size are imaged in high order bright field and weak beam dark field in A and B respectively. Evidence of coalescence of several closely spaced precipitates can be seen in region C. The pocked appearance of the matrix shows black/white contrast dependent on $\vec{g}$ and the mode of imaging (i.e. BF or DF), indicative of point defect clusters.

Fig. 21. Wide images due to surface strain relaxation from small disc-shaped precipitates located near the specimen surface can be seen in this BF image. Further support that the pocked background is due to point defect clusters can be gained by observing their contrast reversals across extinction contours.

Fig. 22. The small disc-like precipitates in a [001] oriented specimen are seen face-on as well as edge-on in this BF image. Trace ' analysis reveals the precipitates to lie on {001} planes. The size and contrast (i.e. line of no contrast LC perpendicular to $\vec{g}$) indicate these to be coherent precipitates with resulting lattice displacements normal to their plane.

Fig. 23. STEM/EDAX spectra failed to differentiate between the composition of the matrix material near a small disc-shaped precipitate (A) and the precipitate itself (B). However, no traces

of elements extrinsic to $Ca_3Ga_2Ge_3O_{12}$ (except the usual Fe and Cu) were found, indicating these defects to be intrinsic to the CGGG system.

Fig. 24. Small loop-like precipitates 0.1μ or less in diameter are seen in the vicinity of the larger (0.5μ) microsegregates, some of which show evidence of the light spheres displaced from their centers. Note the denuded region on either side of the larger microsegregates, suggesting the small disc-like precipitates to be a preliminary stage in the formation of the larger chemical defects. The perspective in the BF image is along [001].

A

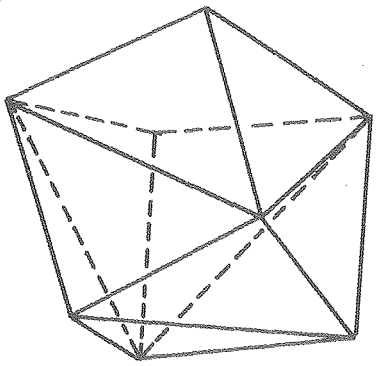

B

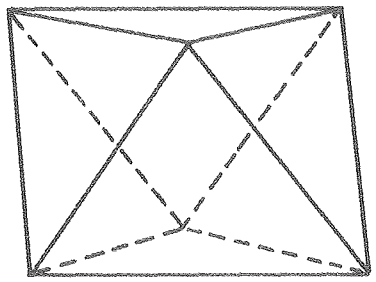

C

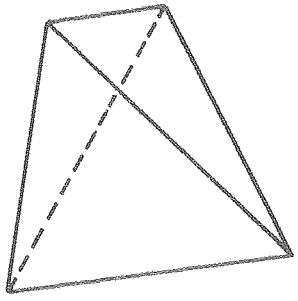

XBL 788-5603

Fig. 1

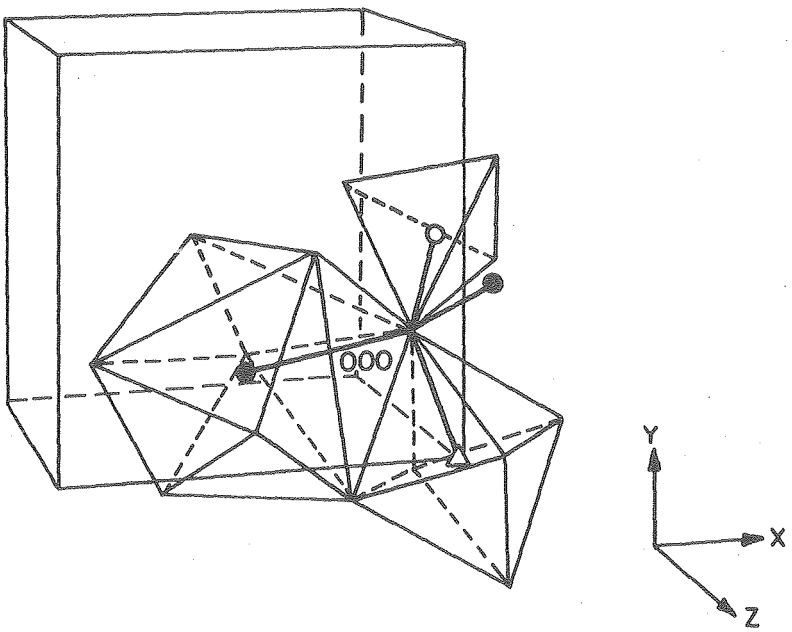

△ Ga^{3+} (a) at $(00\frac{1}{2})$

○ Ge^{4+} (d) at $(0\frac{1}{4}\frac{3}{8})$

● Ca^{2+} (c) at $(-\frac{1}{4}\frac{1}{8}\frac{1}{2})$
and at $(0\frac{1}{4}\frac{5}{8})$

XBL788-5604

Fig. 2

A

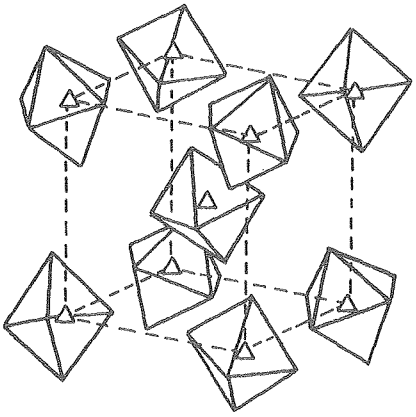

B

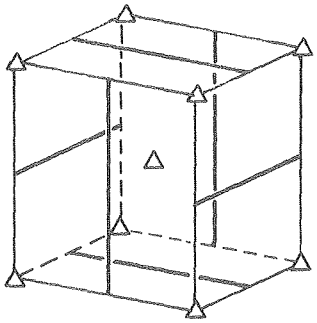

C

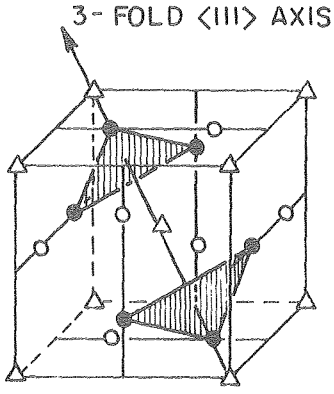

XBL788-5606

Fig. 3

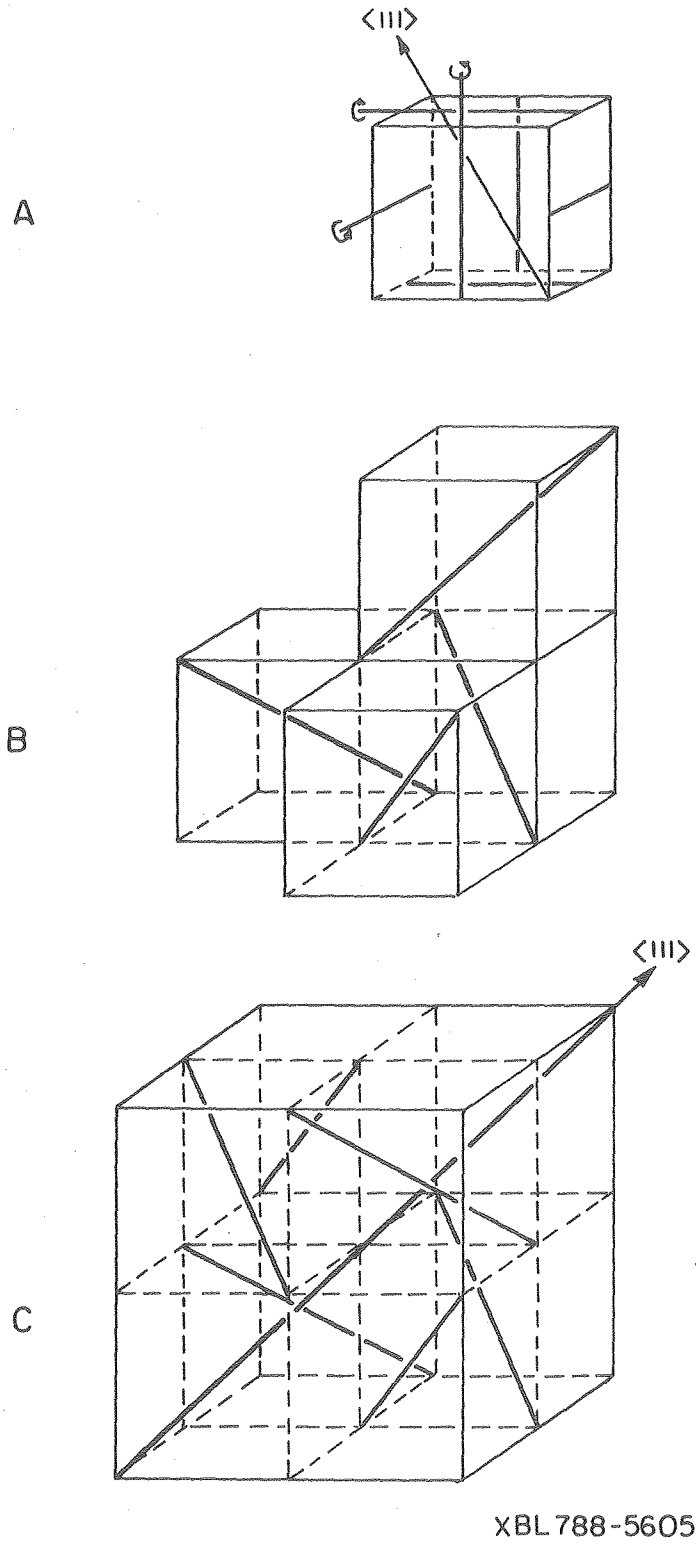

Fig. 4

A

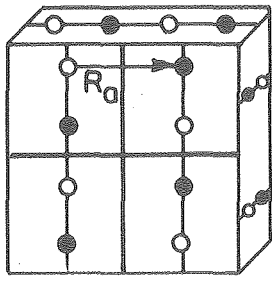

B

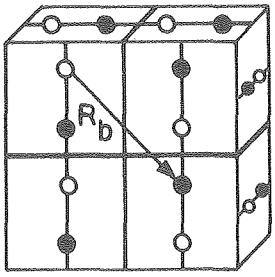

C

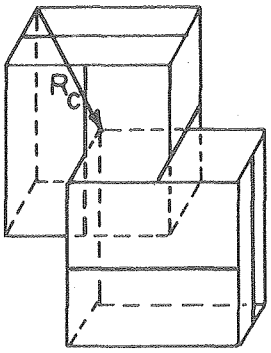

XBL 788-5607

Fig. 5

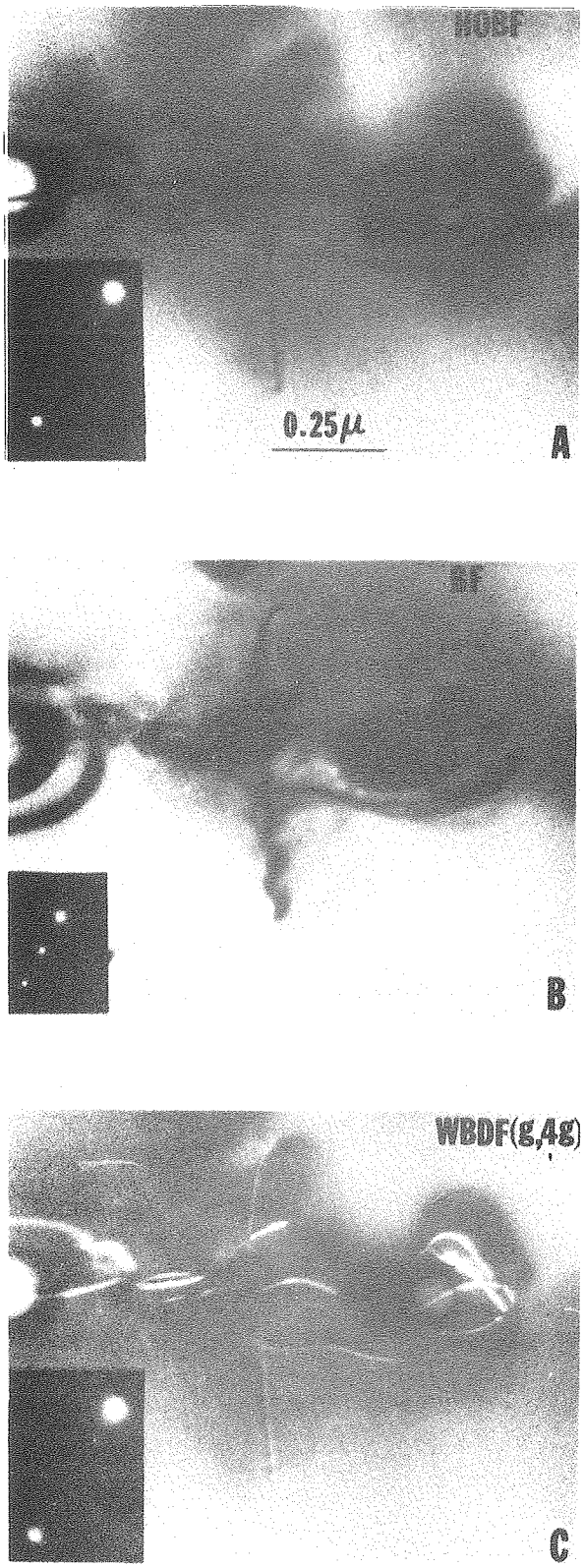

XBB 788-9497

Fig. 6

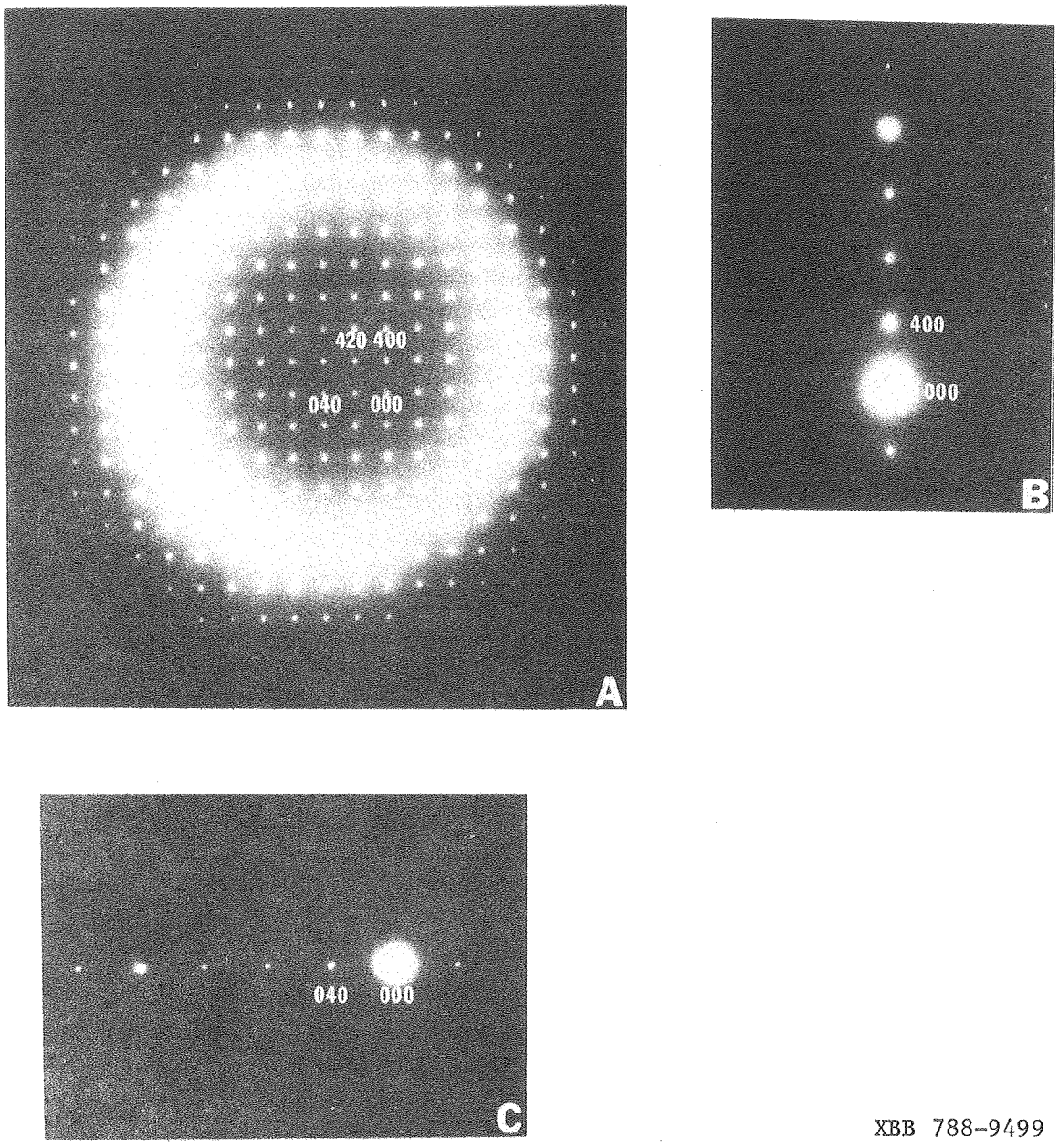

XBB 788-9499

Fig. 7

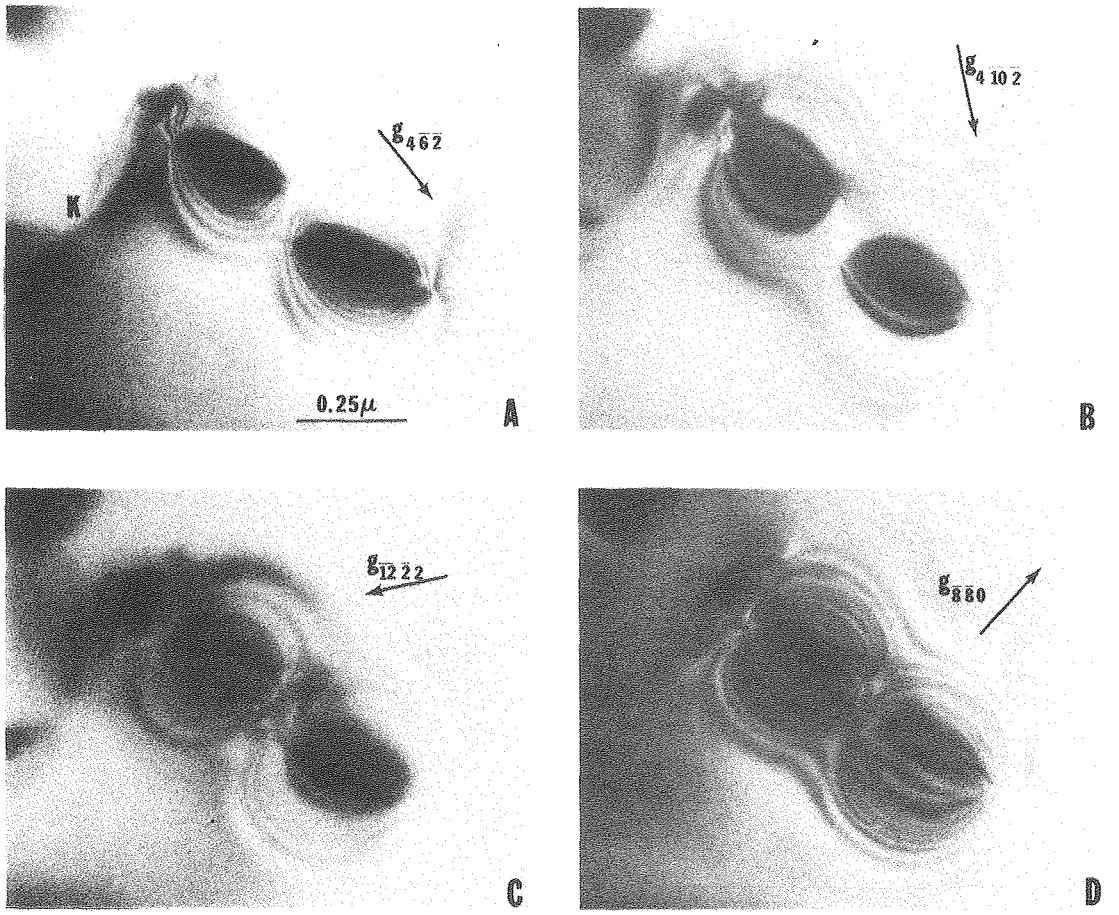

XBB 784-4979

Fig. 8

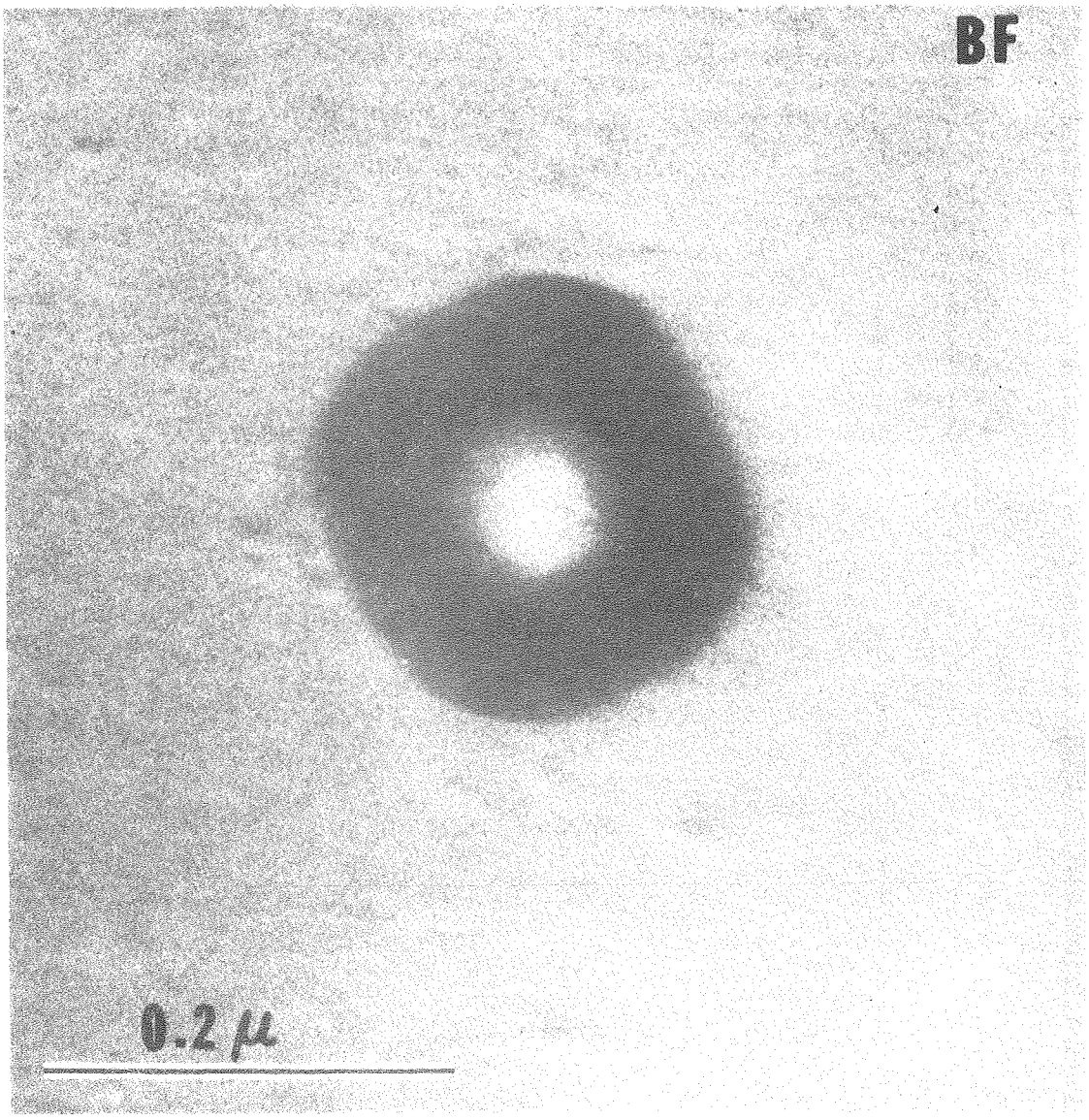

XBB 788-9506

Fig. 9

XBB 788-9505

Fig. 10

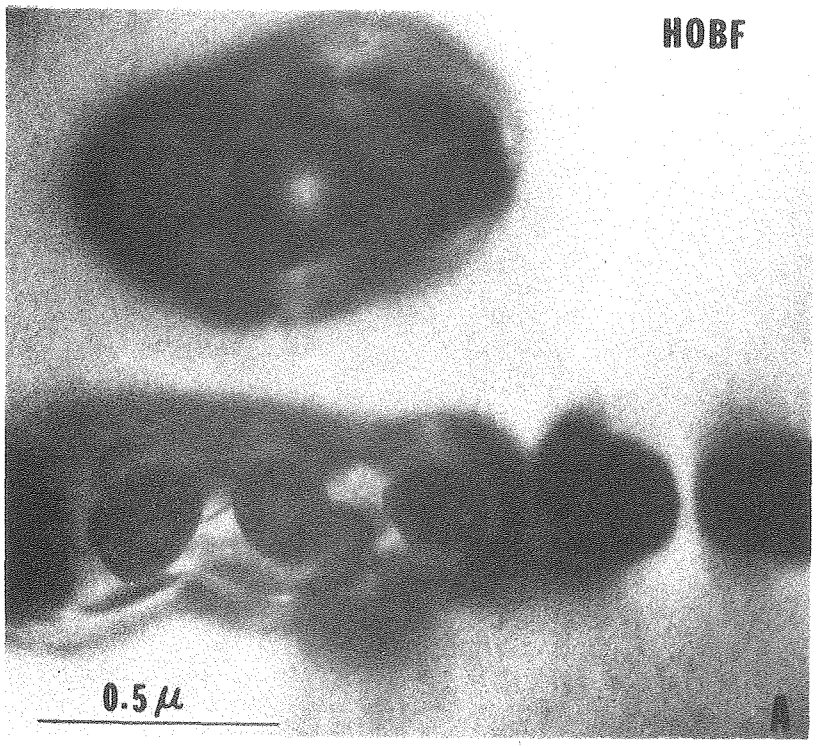

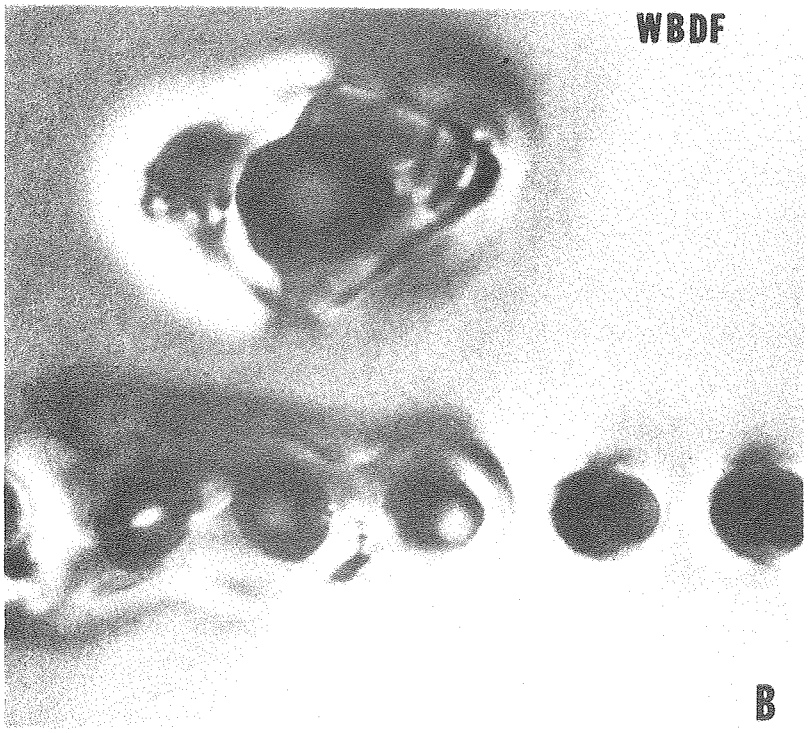

XBB 788-9500

Fig. 11

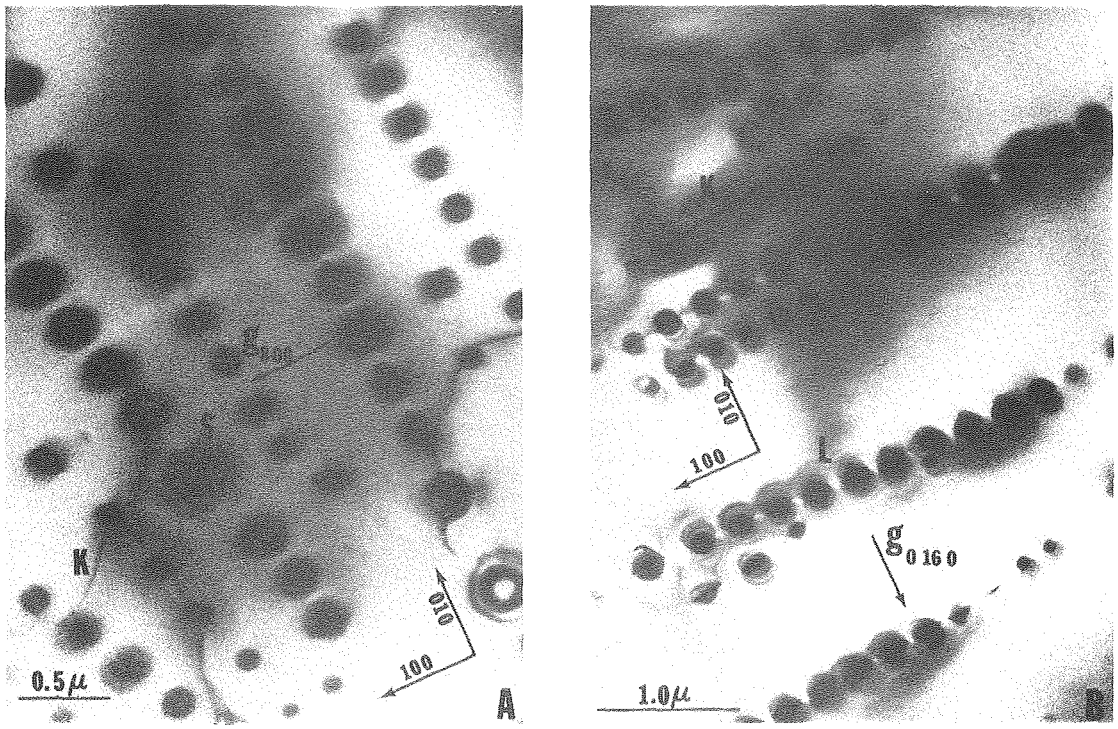

XBB 788-9496

Fig. 12

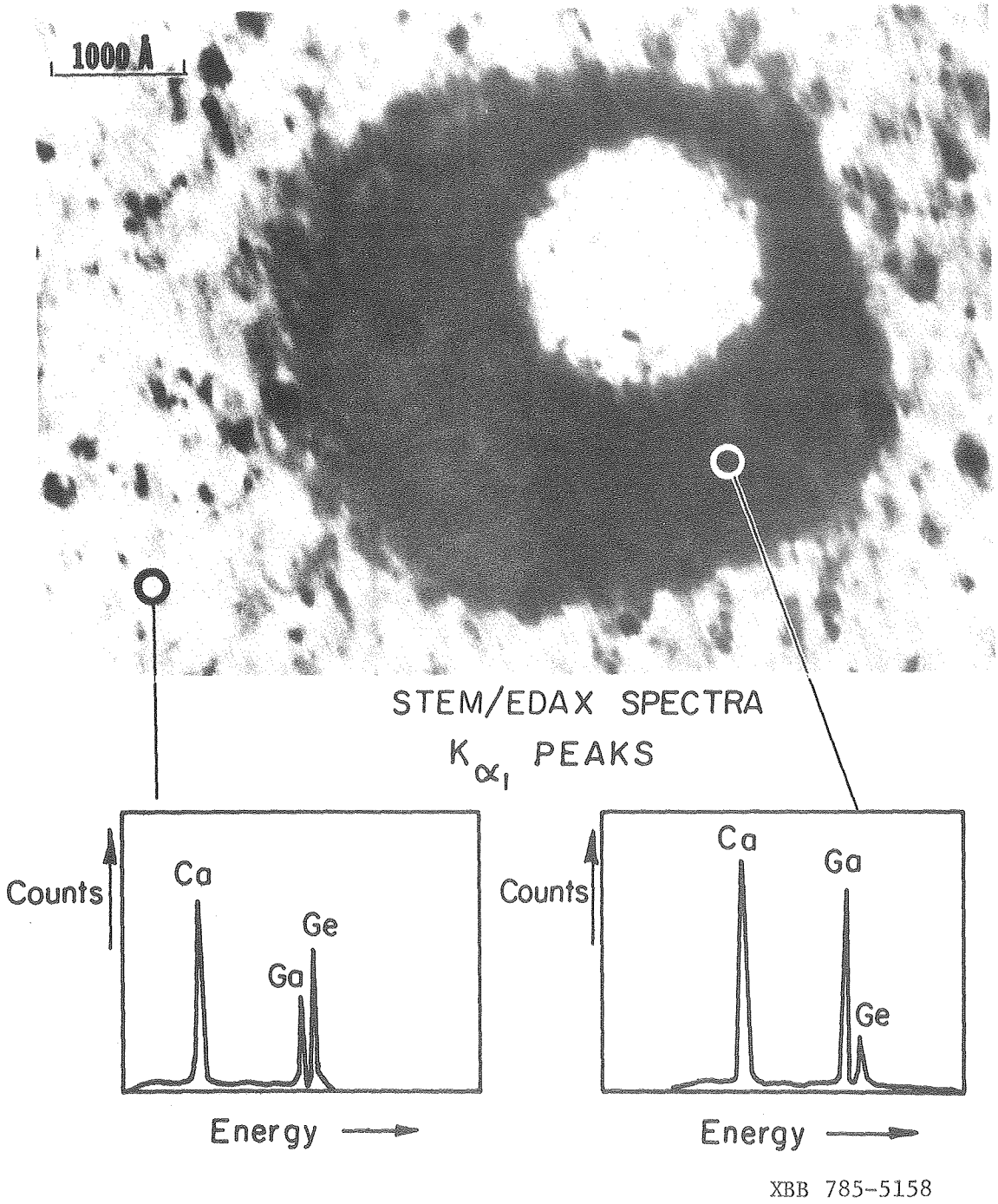
1000 Å
STEM/EDAX SPECTRA
K_{α_1} PEAKS
Counts
Ca
Ge
Ga
Energy
Counts
Ca
Ga
Ge
Energy
XBB 785-5158

Fig. 13

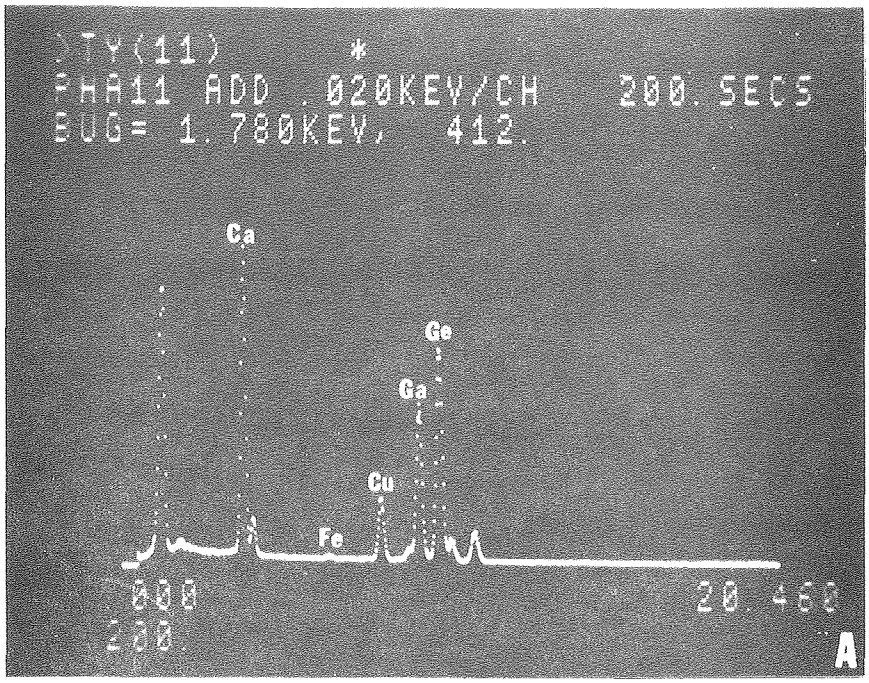

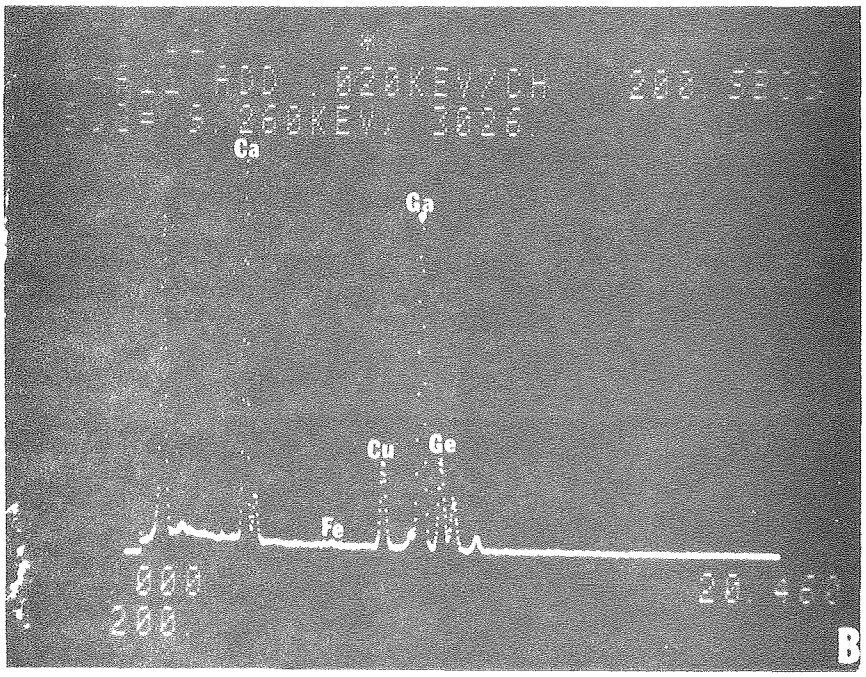

CBB 788-9503

Fig. 14

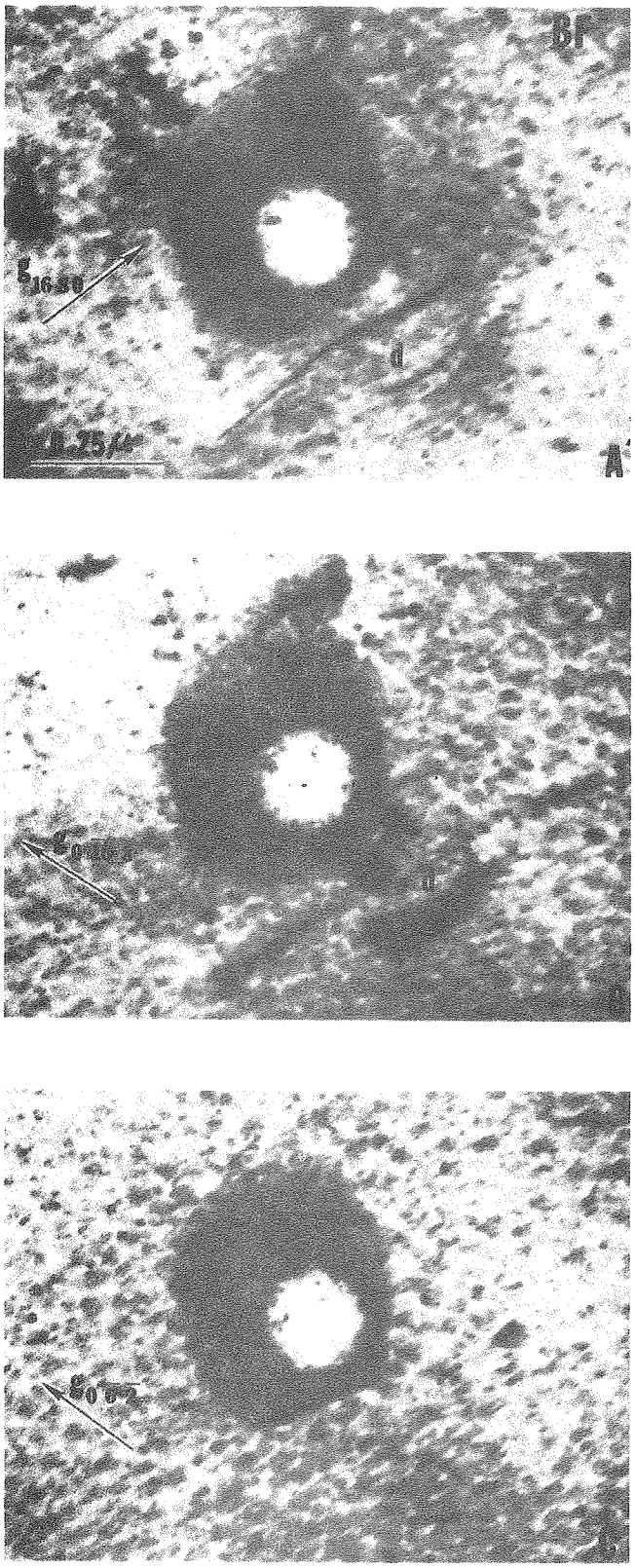

XBB 788-9495

Fig. 15

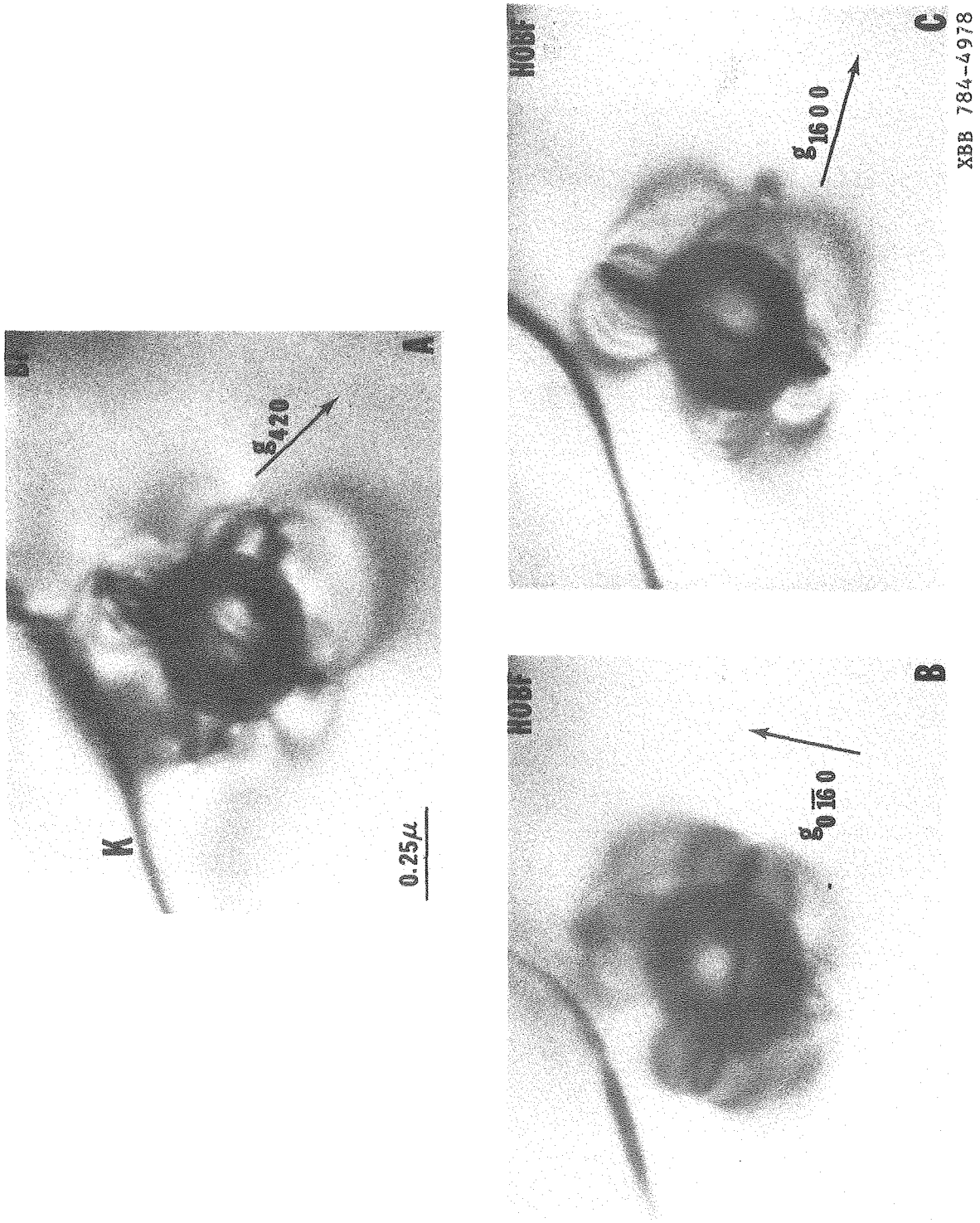

Fig. 16

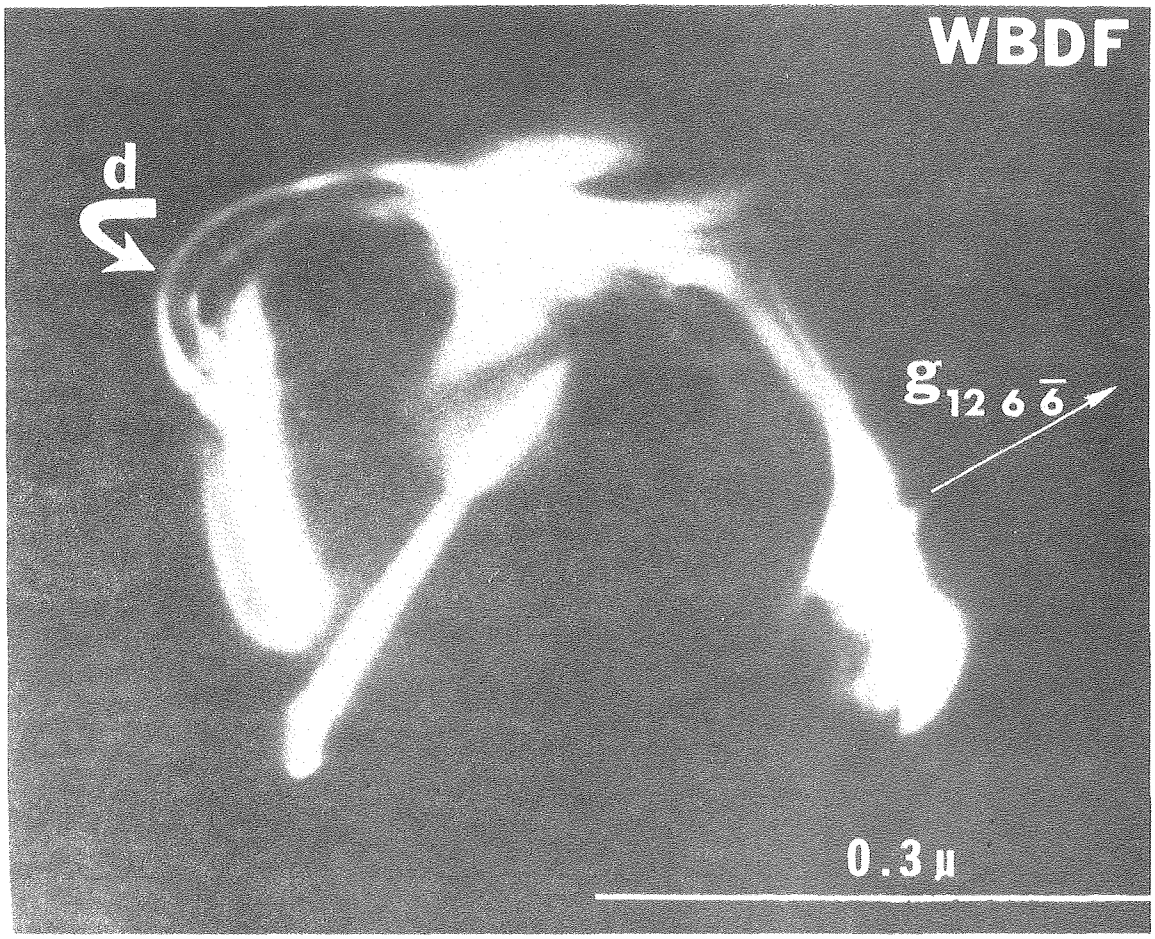

XBB 784-4976

Fig. 17

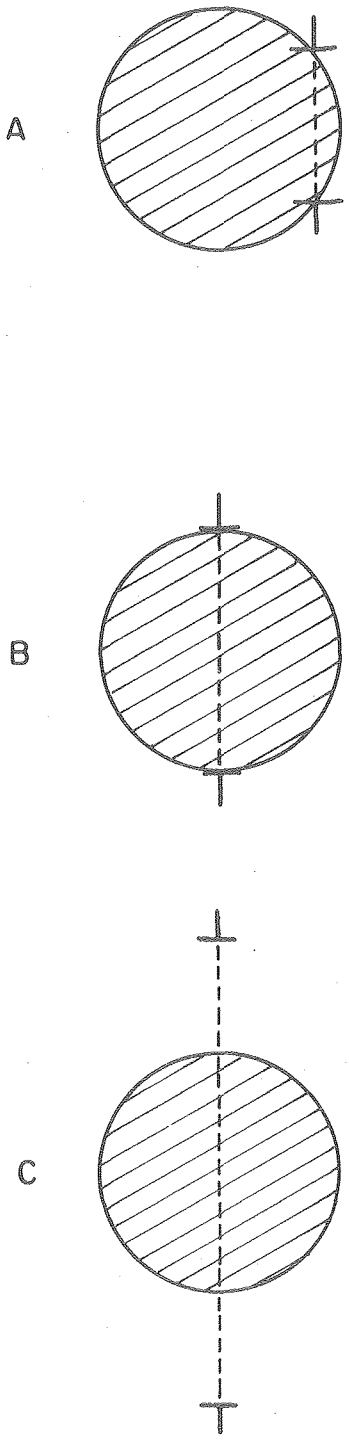

XBL 788-5601

Fig. 18

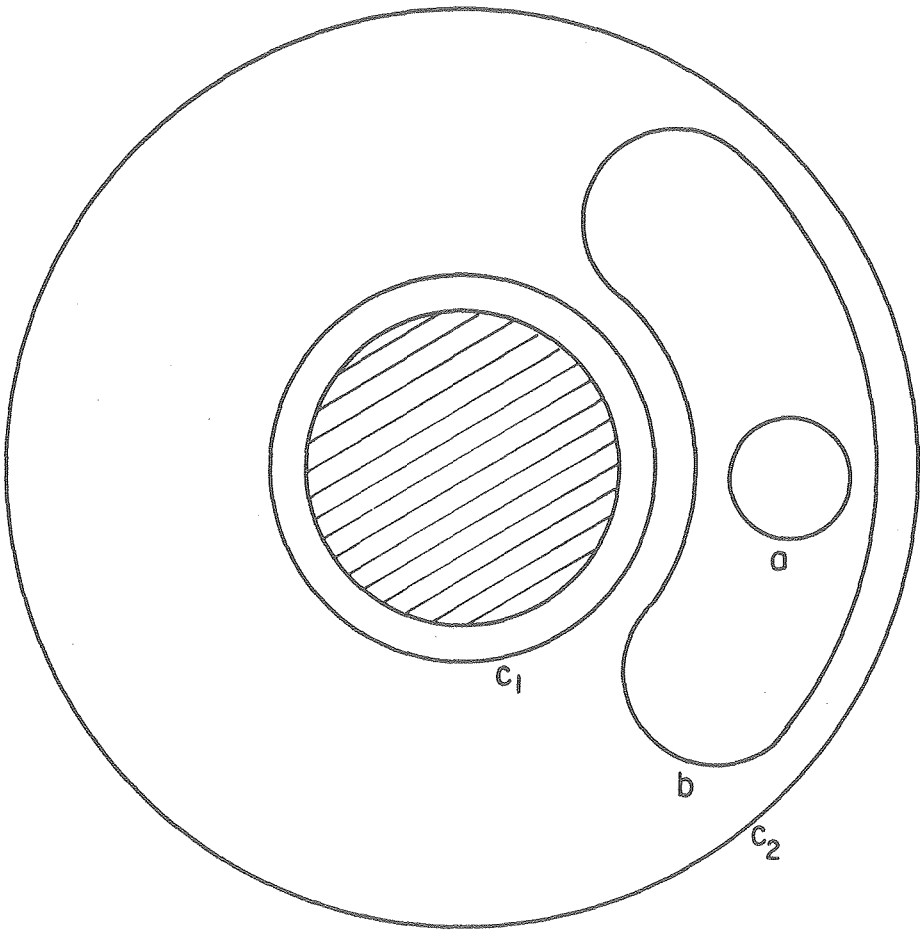

XBL 788-5602

Fig. 19

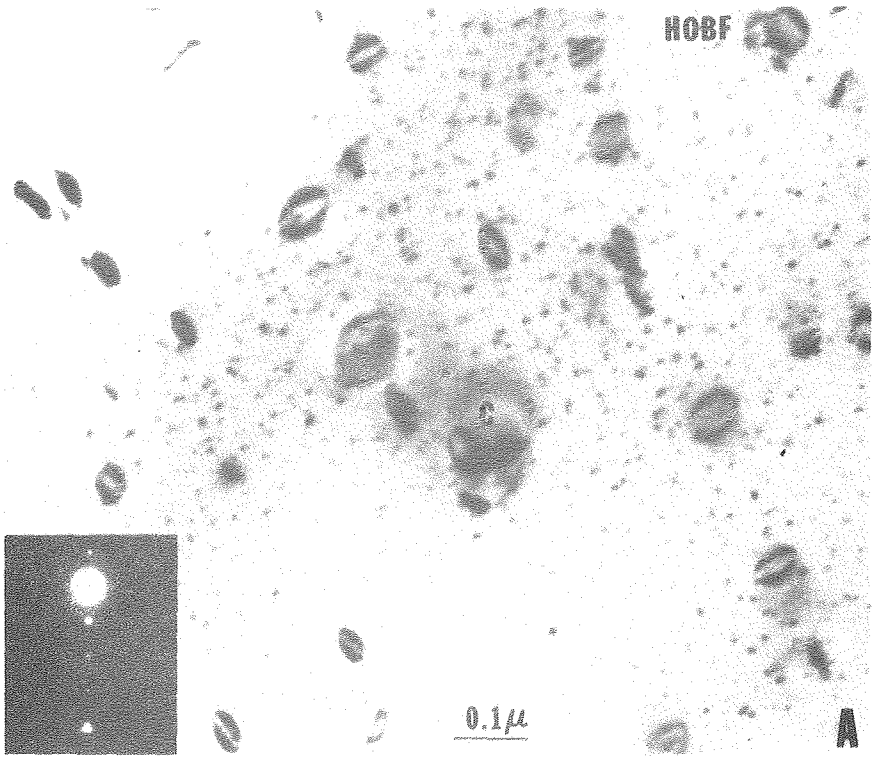

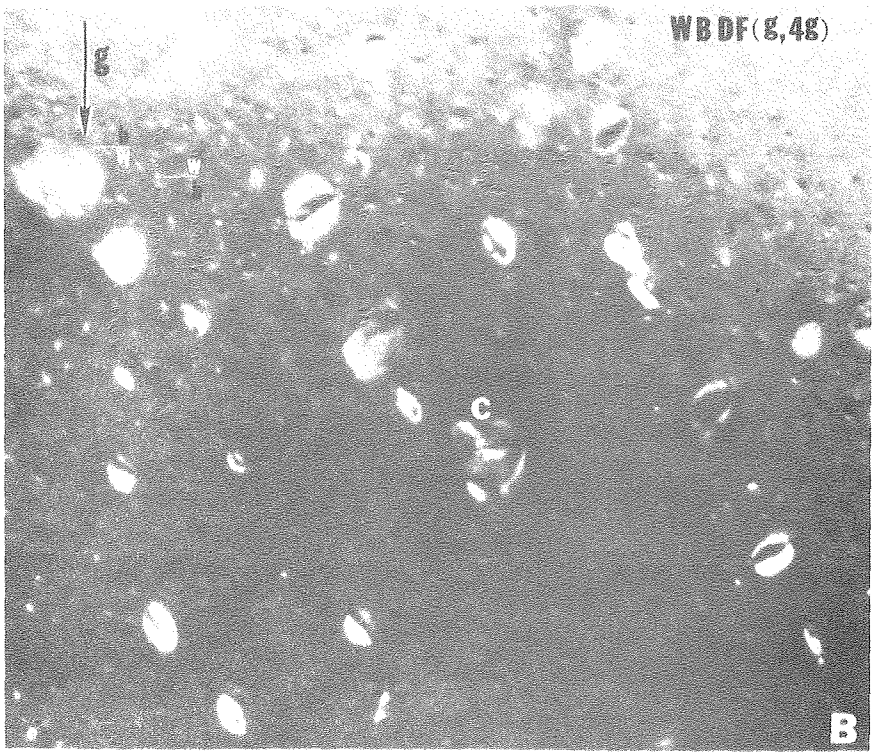

XBB 788-9494

Fig. 20

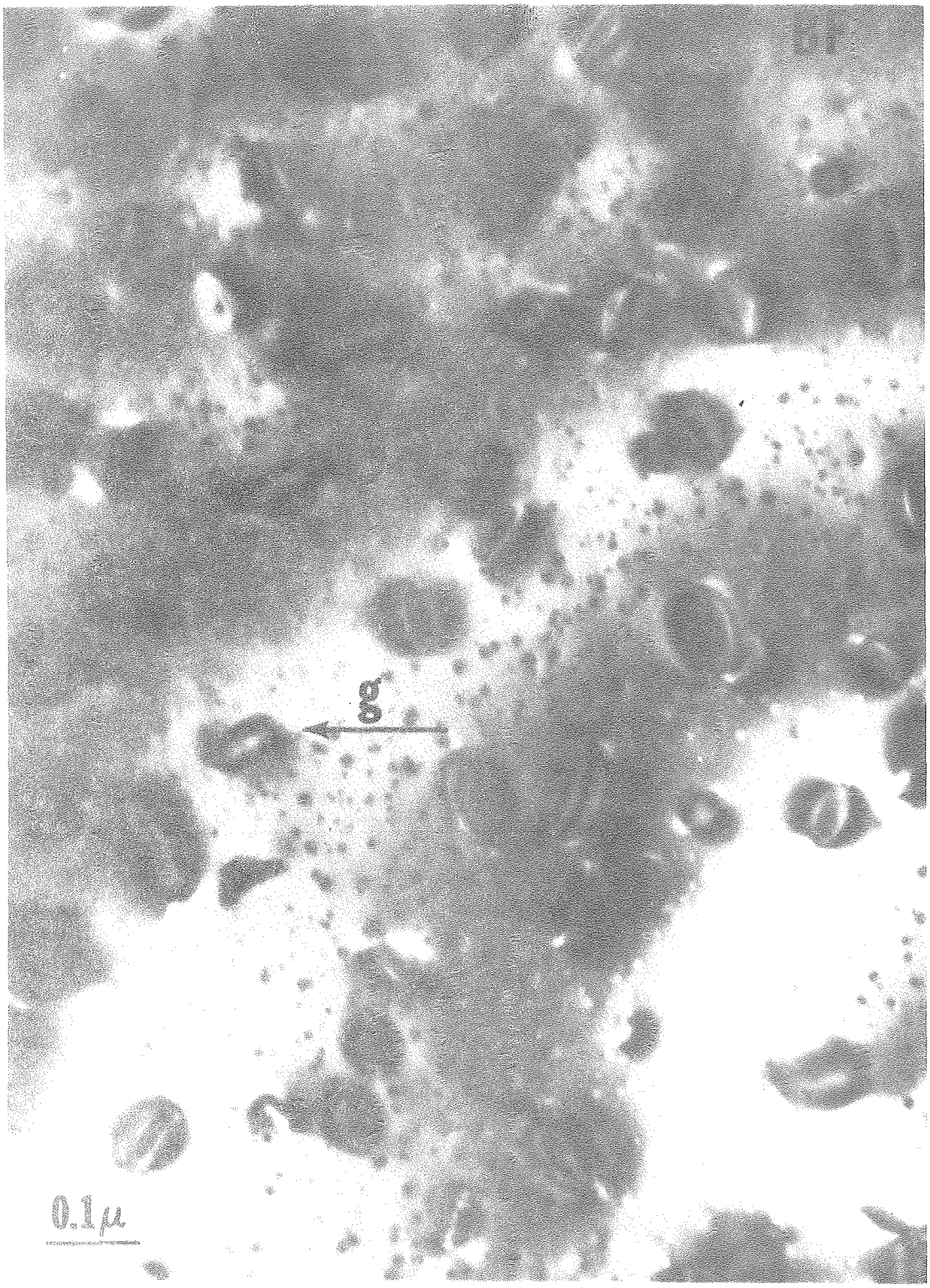

XBB 788-9502

Fig. 21

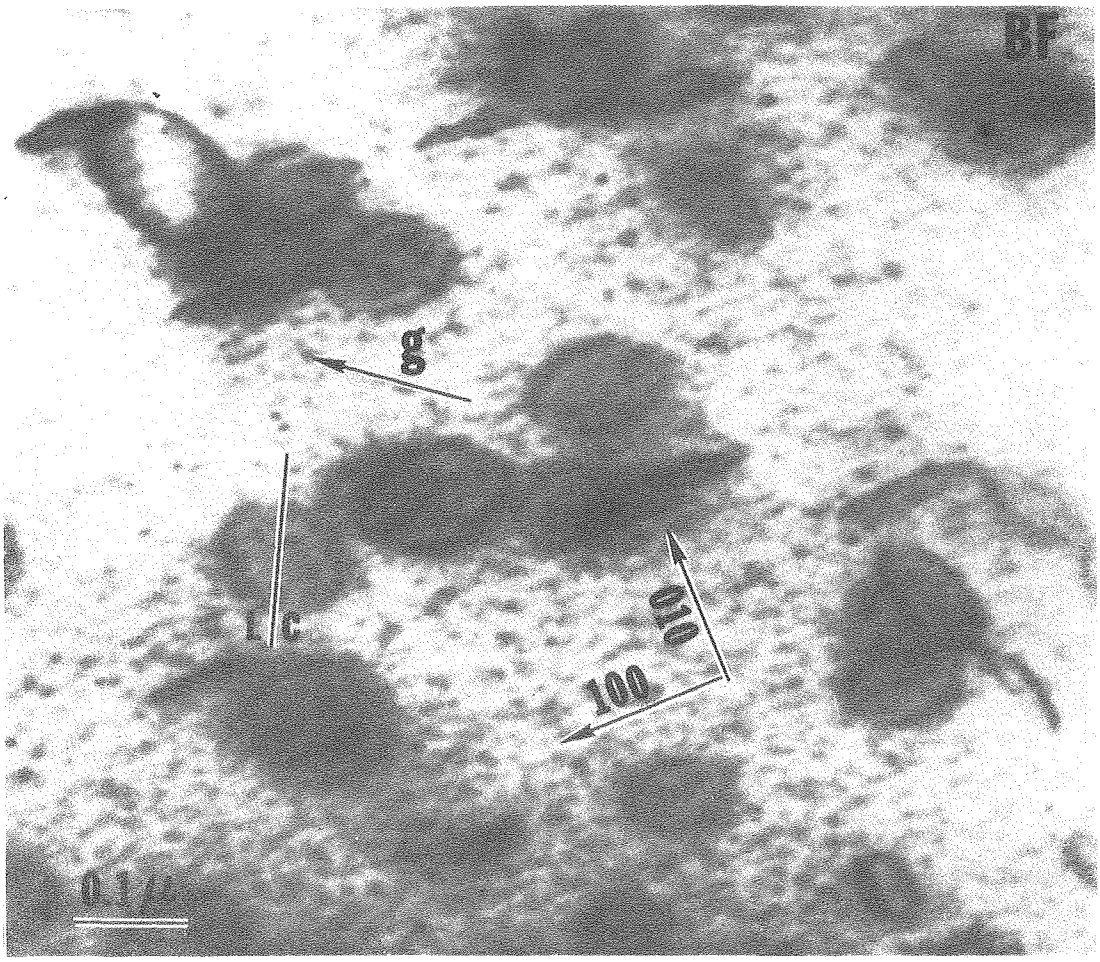

XBB 788-9498

Fig. 22

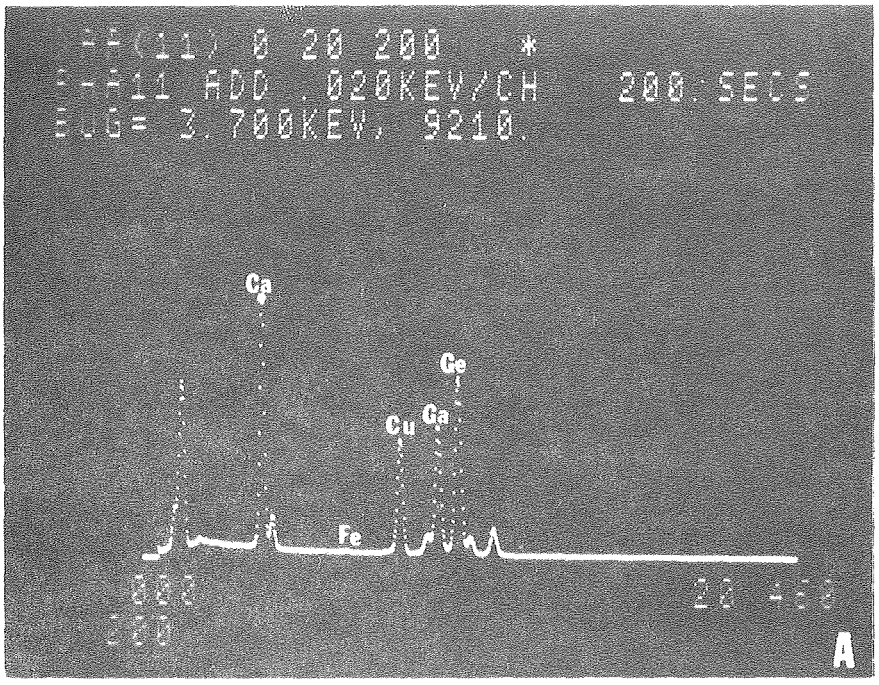

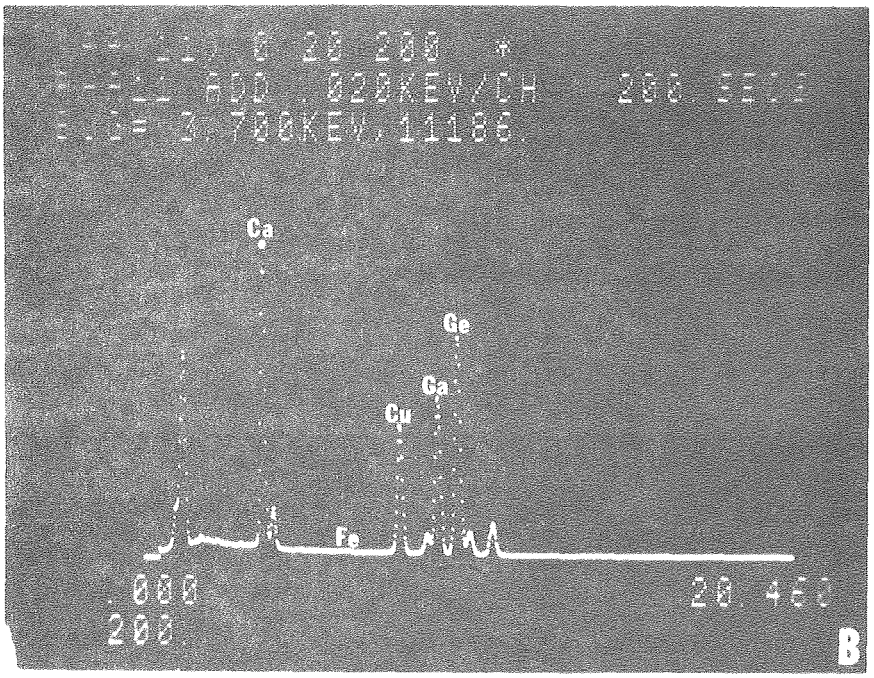

CBB 788-9504

Fig. 23

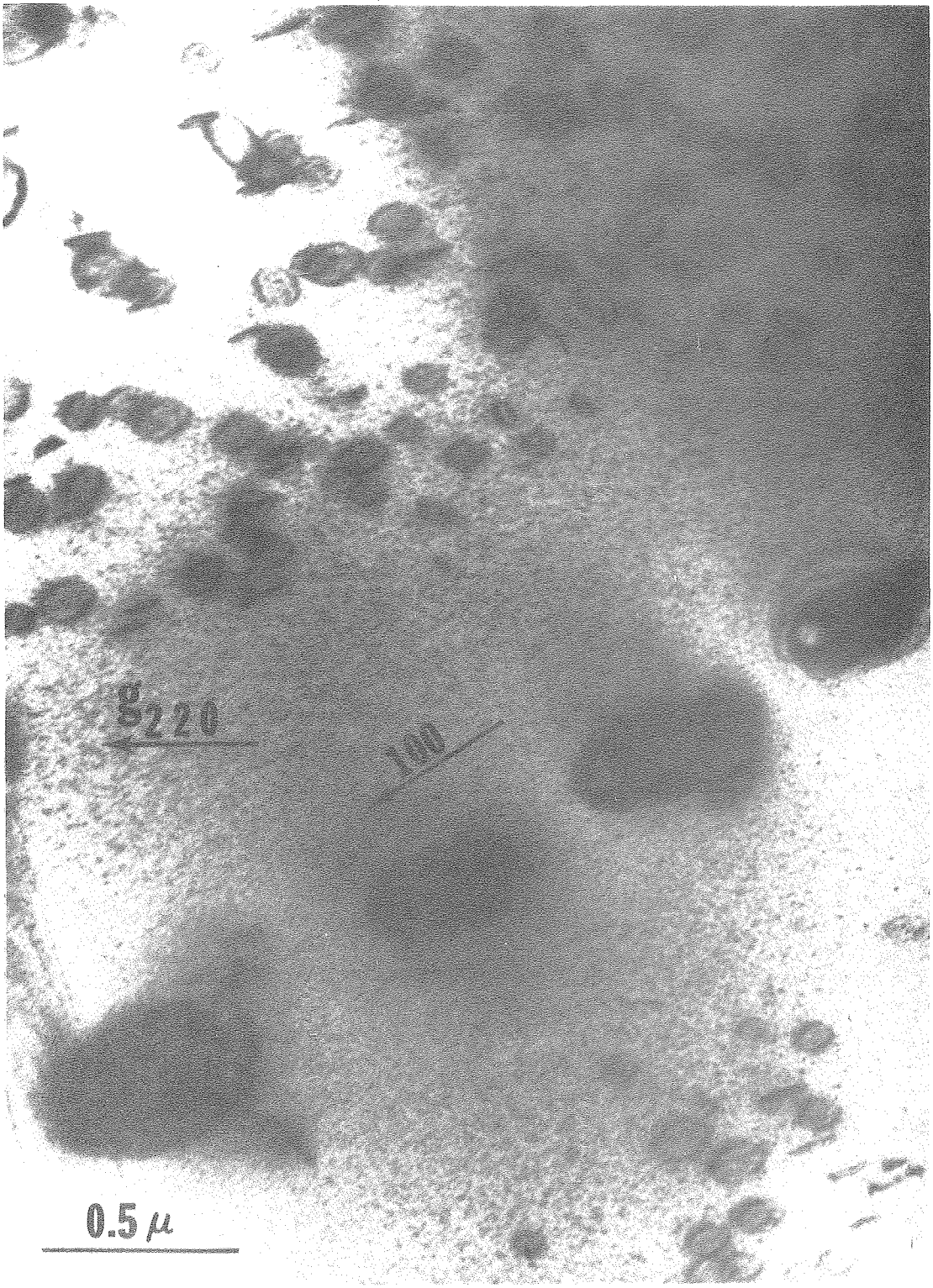

XBB 788-9501

Fig. 24

This report was done with support from the Department of Energy. Any conclusions or opinions expressed in this report represent solely those of the author(s) and not necessarily those of The Regents of the University of California, the Lawrence Berkeley Laboratory or the Department of Energy.

TECHNICAL INFORMATION DEPARTMENT
LAWRENCE BERKELEY LABORATORY
UNIVERSITY OF CALIFORNIA
BERKELEY, CALIFORNIA 94720